Computer Methods in Applied Mechanics and Engineering 437 (2025) 117794

Contents lists available at ScienceDirect

Comput. Methods Appl. Mech. Engrg.

journal homepage: www.elsevier.com/locate/cma

Coupled semi-Lagrangian and poroelastic peridynamics for modeling hydraulic fracturing in porous media

Zirui Lu [a], Fan Zhu [b,*], Yosuke Higo [a], Jidong Zhao [c]

[a] Department of Civil and Earth Resources Engineering, Kyoto University, Kyoto, Japan
[b] Department of Urban Management, Kyoto University, Kyoto, Japan
[c] Department of Civil and Environmental Engineering, Hong Kong University of Science and Technology, HKSAR, China

ARTICLE INFO

Keywords:
Porous media
Fracture
Fluid-solid interaction
Peridynamics
Leak-off

ABSTRACT

A novel peridynamics-based computational approach is proposed for modeling hydraulic fracturing in porous media with consideration of leak-off effect. The approach features the use of the semi-Lagrangian peridynamics (PD) formulation which simulates fluid, and the poroelastic PD formulation which simulates deformation and fracture of porous solid with seepage flow. A new porous flow equation, which suits in the state-based PD, is derived using Non-local Differential Operators (NDOs) and based on Darcy's law. A novel fluid-solid interface (FSI) model is proposed by coupling the two PD formulations. The FSI considers both the hydraulic forces applied on the fracture surfaces and the leak-off of fluid into poroelastic media. The proposed model is verified by benchmark cases including one-dimensional consolidation, 2-D Mandel's problem, and constant head permeability test, for which analytical solutions are available. It is then applied to simulate hydraulic fracturing in porous media with consideration of the fluid leak-off and benchmarked with the analytical solutions from the Kristianovich-Geertsma-de Klerk (KGD) model and Carter's equation. Simulation results demonstrate that the proposed model can reasonably capture the porous flow and pore pressure variation with solid deformation, the mass exchange between the fluid in the fracture and porous flow, and the fracture propagation in the porous media with concurrent leak-off.

1. Introduction

Hydraulic fracturing plays a vital role in many engineering operations such as shale gas exploitation [1,2], Enhanced Geothermal System (EGS) [3], and abrasive waterjet cutting [4]. A typical hydraulic fracturing process involves injection of pressurized fluid into a solid which creates and extends fractures. The performance of fracturing directly influences the efficiency of those operations. On the other hand, hydraulic fracturing needs to be carefully controlled in some engineering operations. In the EGS, the leakage of fracking water into existing faults may lead to unwanted earthquakes which could be large sometimes [5,6]. In geological carbon sequestration and wastewater disposal, hydraulic fracturing is to be avoided as it may cause leakage of the storage fluid. Assessment of potential hydraulic fracturing is therefore a pivotal task. When fracturing geomaterials, the fluid is injected into porous rock medium and some of the fluid infiltrate into the surrounding rock nearby the fracture. This phenomenon, known as leak-off, is a critical aspect associated with the fracturing process because it can significantly affect the initiation and propagation of fractures and the operational performance of hydraulic fracturing [7–9].

* Corresponding author.
E-mail address: zhu.fan.7m@kyoto-u.ac.jp (F. Zhu).

https://doi.org/10.1016/j.cma.2025.117794
Received 8 November 2024; Received in revised form 30 December 2024; Accepted 23 January 2025

0045-7825/© 2025 The Authors. Published by Elsevier B.V. This is an open access article under the CC BY license (http://creativecommons.org/licenses/by/4.0/).

A variety of numerical approaches are developed for simulation and study of hydraulic fracturing process. They can be generally divided into mesh-based and meshfree methods. The former category mainly includes boundary element method [10–12] and finite element-based methods [13–16]. Notably, Zhang et al. [11] presented a boundary element model for hydraulic fracturing where fluid flow is solved by lubrication equation. Cheng et al. [12] introduced a coupled boundary element method and finite volume method for modeling hydraulic fracturing near a wellbore in impermeable rock. Mohammadnejad and Khoei [16] developed a coupled approach for modeling hydraulic fractures in porous media based on extended finite element method and cohesive crack model. Settgast et al. [13] described a coupled finite element/finite volume approach for modeling hydraulic fracturing in porous media where the leak-off is considered via a sink term given by the Cater's leak-off method. Nonetheless, the mesh-based continuum methods often encounter difficulties when significant discontinuities are introduced into the model by complex evolving fractures. The meshfree methods, such as distinct element method [17–19], smoothed particle hydrodynamics [20,21], material point method [22,23], and peridynamics (PD) [24–29], have received increasing attention for fluid-driven fracture modeling. In particular, the PD method [30,31] is considered advantageous for addressing problems that involve significant discontinuities, owning to the nature that it is formulated on integral-differentiation governing equations. The method has been demonstrated its considerable versatility in simulating fracturing in a variety of materials such as rock [32,33], glass [34], metal [35], and membrane [36] under different failure modes such as fatigue [37], hydraulic forces [24,26,27], blasting [33], and corrosion [38,39]. The PD theory was originally developed for modeling fracturing in solids. The original bond-based peridynamics [30] is known to be restricted to certain materials. The later developed state-based peridynamics (SBPD) [31] has nonetheless offered opportunities to model a variety of materials. The SBPD can be further classified into ordinary and non-ordinary types where the latter allows convenient implementation of classical material constitutive models into the PD framework.

Given the advantages of the PD theory in modeling problems involving discontinuities, the theory has been extended for simulation of hydraulic fracturing problems. Zhang et al. [40] proposed an ordinary state-based peridynamics approach for modeling hydraulic fracturing where fluid flow is described by the cubic law on crack elements. Qin et al. [41] studied the hydraulic fracture of layered rock using bond-based PD and modeled the fluid flow in fracture as one-dimensional seepage based on the parallel-plate flow theory [42]. Coupled methods have been developed where the PD theory is employed for modeling fracturing in solid with other numerical methods used for simulating fluid flow [27,43–47]. Recently, a novel branch of the PD theory, namely the semi-Lagrangian formulation [48], was developed to simulate fluid [49,50]. The formulation is also known as the updated-Lagrangian formulation. The semi-Lagrangian formulation is adaptive to large deformation of material, as the neighborhood of each material point is updated at every time step and material response is calculated based on current configuration instead of the initial configuration. The Navier–Stokes equations is solved non-locally using the PD differential operator [51,52], and the fluid-solid interaction can be established by proper coupling between the semi- and total-Lagrangian formulations of PD [53]. Two types of non-local operators have been developed for solving partial differential equations, namely the peridynamic differential operator (PDO) and the non-local differential operator (NDO) [54]. The PDO was developed as a class of antisymmetric non-local operators derived from non-local balance laws [55–58]. This operator assumes that the function it acts upon is antisymmetric, and both the action and reaction along the bond are considered. Its performance, however, was found to deteriorate when with non-uniform material point discretization [54]. The NDO [59] is derived from the Taylor series expansion of non-local interpolation. It computes the gradient and divergence at the material point as a function of all bonds within a horizon. It has been proved to converge to the local gradient/divergence operator as the horizon approaches zero [59]. Both PDO and NDO are defined without partial derivatives with respect to space, offering unique advantage in solving non-local diffusion problems. NDO has been successfully applied in modeling fluid [49], and subsequently, a coupled semi- and total-Lagrangian approach was proposed [60] for modeling hydraulic fracturing in impermeable solids. Hence, both the fluid and solid can be explicitly modeled within the PD framework. For porous media with seepage flow, the poroelastic peridynamic model has been progressively developed [24,26,61–67]. Katiyar et al. [61] presents a peridynamic model to simulate the porous flow in porous media without considering the mechanical behavior. Turner [63] proposed a SBPD model for porous media based on mixture theory, where the interaction between the fluid and solid phases is explicitly considered. The model implements effective stress principle to capture the fluid induced deformation without accounting for crack initiation. Ouchi et al. [24] developed a fully coupled porous flow and geomechanics model that simultaneously considers both porous flow and fracture flow, along with crack propagation. In this model, the fracture fluid pressure is applied normally to the fracture surface by modifying the force density. The deformation and damage of peridynamic poroelastic material are modeled under various conditions in literature [26,64–67]. However, the existing peridynamics-based methods have dealt with hydraulic fracturing in simplified ways. It was a common approach to directly apply hydraulic pressures on the damaged material points to simulate pressurized fluid in the fractures without explicit simulation of the fluid flow. In most studies, the solid was assumed to be impermeable which only suits in the condition that injection rate is much higher than the rate of fluid infiltration into the porous media. To rigorously model the hydraulic fracturing process in porous media, it is demanded that a numerical model can concurrently simulate the fluid flow inside or outside the fractures, the leak-off and flow in the porous media, as well as the mass exchange between fluid in the fracture and the flow in porous media.

In this paper, a novel peridynamics-based computational approach is proposed for modeling hydraulic fracturing in porous solid. The approach features the coupling of semi-Lagrangian and poroelastic formulations of PD for modeling fluid and porous solid, respectively, in the framework of state-based PD. The explicit modeling of fluid naturally captures fluid flow in complex fracture geometry. For the poroelastic PD formulation, we derive the governing equation for the porous flow based on the NDO and Darcy's law. A new fluid-solid interface (FSI) model is proposed to couple the two formulations while allowing mass transfer from fluid material points into the porous medium. The proposed approach takes into account the fluid leak-off during the fracturing process, and is fully formulated in the PD framework which allows convenient implementation. The mass loss of fracturing fluid can be

quantitatively assessed in the proposed approach. In the following section, the formulations of the poroelastic PD model, the semi-Lagrangian fluid model, and the FSI model are described. Validations of the model and numerical examples are given in Section 3, with discussion and conclusions presented in Section 4.

2. Coupled fluid-poroelastic peridynamics formulation

2.1. Peridynamics theory for solids

In peridynamics, the continuum domain is discretized into a set of Lagrangian elements known as *material points*, each endowed with specific properties and initial conditions. For a given material point $\boldsymbol{x}$, a virtual spherical space, denoted as the *family* $\Omega_{\boldsymbol{x}}$, is defined by a radius termed *horizon* δ (Fig. 1). All material points within $\Omega_{\boldsymbol{x}}$ are considered *neighbors* of $\boldsymbol{x}$, and a peridynamic bond is established between $\boldsymbol{x}$ and each of its neighbors to characterize the interactions among them. The generalized equation of motion of state-based PD is given by

$$\rho(\boldsymbol{x})\ddot{\boldsymbol{u}}(\boldsymbol{x},t)=\int_{\Omega_{\boldsymbol{x}}}\left[\mathbf{T}(\boldsymbol{x},t)\langle\boldsymbol{x}'-\boldsymbol{x}\rangle-\mathbf{T}(\boldsymbol{x}',t)\langle\boldsymbol{x}-\boldsymbol{x}'\rangle\right]dV_{\boldsymbol{x}'}+\mathbf{b}(\boldsymbol{x},t) \tag{1}$$

where $\rho(\boldsymbol{x})$ represents the density of material point $\boldsymbol{x}$, $\boldsymbol{u}$ denotes displacement, $\mathbf{b}$ represents body force density and $dV_{\boldsymbol{x}'}$ denotes the volume of neighbor point $\boldsymbol{x}'$. In state-based PD, the force state $\mathbf{T}\langle\boldsymbol{x}'-\boldsymbol{x}\rangle$ describes the force acting on the vector $\langle\boldsymbol{x}'-\boldsymbol{x}\rangle$ originating from material point $\boldsymbol{x}$ and pointing to a neighbor point $\boldsymbol{x}'$. For the linear peridynamic solid (LPS) material model, which is a non-local analogy to the linear elastic material model, the force state is calculated by

$$\mathbf{T}\langle\boldsymbol{x}'-\boldsymbol{x}\rangle=t\frac{\mathbf{Y}}{\|\mathbf{Y}\|} \tag{2}$$

where t is the scalar force state representing the magnitude of bond force density, and $\mathbf{Y}$ is the deformation vector given by the current configuration. The scalar force state [24,31] is defined as

$$t=\begin{cases}\dfrac{2\left(K-\frac{\mu}{3}\right)\vartheta\langle\boldsymbol{x}\rangle}{\bar{m}\langle\boldsymbol{x}\rangle}\omega\langle\|\boldsymbol{\xi}\|\rangle\|\boldsymbol{\xi}\|+\dfrac{8\mu}{\bar{m}\langle\boldsymbol{x}\rangle}\omega\langle\|\boldsymbol{\xi}\|\rangle\underline{\mathrm{e}}^{d} & \text{for 2D,}\\ \dfrac{3K\vartheta\langle\boldsymbol{x}\rangle}{\bar{m}\langle\boldsymbol{x}\rangle}\omega\langle\|\boldsymbol{\xi}\|\rangle\|\boldsymbol{\xi}\|+\dfrac{15\mu}{\bar{m}\langle\boldsymbol{x}\rangle}\omega\langle\|\boldsymbol{\xi}\|\rangle\underline{\mathrm{e}}^{d} & \text{for 3D}\end{cases} \tag{3}$$

where K and μ represent bulk modulus and shear modulus, respectively, and $\boldsymbol{\xi}$ is the bond vector from material point $\boldsymbol{x}$ to neighbor $\boldsymbol{x}'$ in the reference configuration. Note that the 2D condition refers to the plane strain condition and all subsequent simulations assume the plane strain condition. Hydraulic fracturing under plane stress condition is considered uncommon in engineering practice. The influence function ω is taken as $\omega=e^{-\left(\frac{\|\boldsymbol{\xi}\|}{0.4\delta}\right)^2}$, which is known as the Gaussian type and is reported to improve accuracy and numerical stability [68]. The weighted volume $\bar{m}$ and dilatation ϑ are defined by

$$\bar{m}\langle\boldsymbol{x}\rangle=\int_{\Omega_{\boldsymbol{x}}}\omega\langle\|\boldsymbol{\xi}\|\rangle\|\boldsymbol{\xi}\|^2dV_{\boldsymbol{x}'} \tag{4}$$

$$\vartheta\langle\boldsymbol{x}\rangle=\begin{cases}\dfrac{2}{\bar{m}\langle\boldsymbol{x}\rangle}\displaystyle\int_{\Omega_{\boldsymbol{x}}}\omega\langle\|\boldsymbol{\xi}\|\rangle\|\boldsymbol{\xi}\|\underline{\mathrm{e}}dV_{\boldsymbol{x}'} & \text{for 2D}\\ \dfrac{3}{\bar{m}\langle\boldsymbol{x}\rangle}\displaystyle\int_{\Omega_{\boldsymbol{x}}}\omega\langle\|\boldsymbol{\xi}\|\rangle\|\boldsymbol{\xi}\|\underline{\mathrm{e}}dV_{\boldsymbol{x}'} & \text{for 3D}\end{cases} \tag{5}$$

where $\underline{\mathrm{e}}$ is the scalar extension state of a bond composed of an isotropic part $\underline{\mathrm{e}}^{i}$ and a deviatoric part $\underline{\mathrm{e}}^{d}$, which are expressed by $\underline{\mathrm{e}}=\underline{\mathrm{e}}^{i}+\underline{\mathrm{e}}^{d}=\|\mathbf{Y}\|-\|\boldsymbol{\xi}\|$ and $\underline{\mathrm{e}}^{d}=\underline{\mathrm{e}}-\frac{\vartheta\langle\boldsymbol{x}\rangle\|\boldsymbol{\xi}\|}{2}$ for 2D, $\underline{\mathrm{e}}-\frac{\vartheta\langle\boldsymbol{x}\rangle\|\boldsymbol{\xi}\|}{3}$ for 3D, respectively.

2.2. Poroelastic PD model

The poroelastic PD model is intended for simulation of single-phase flow within a porous medium, where both the solid and fluid phases coexist at each material point. The mass conservation equation for the porous flow is expressed as

$$\frac{\partial}{\partial t}\left(\rho_f(\boldsymbol{x},t)\phi(\boldsymbol{x},t)\right)=-\nabla\cdot\left(\rho_f(\boldsymbol{x},t)\boldsymbol{q}(\boldsymbol{x},t)\right)+R(\boldsymbol{x},t) \tag{6}$$

where ρ_f is the density of the fluid phase, ϕ represents the porosity of the porous medium, $\boldsymbol{q}$ represents the volumetric flux, R denotes the mass change rate of source/sink, $\nabla\cdot$ denotes the divergence operator. According to Darcy's law, the volumetric flux is computed by

$$\boldsymbol{q}(\boldsymbol{x},t)=-\frac{k}{\bar{\mu}}\nabla\otimes\boldsymbol{\Phi}(\boldsymbol{x},t) \tag{7}$$

where k is the intrinsic permeability of the porous medium, $\bar{\mu}$ is the dynamic viscosity of fluid, $\boldsymbol{\Phi}$ is the potential field, $\nabla\otimes$ is the gradient operator. In the present study, the potential $\boldsymbol{\Phi}$ takes into account only the pressure head and gravity head, with the assumption that porous flow is slow so that the velocity head is negligible. To derive the peridynamic form of the volumetric flux,

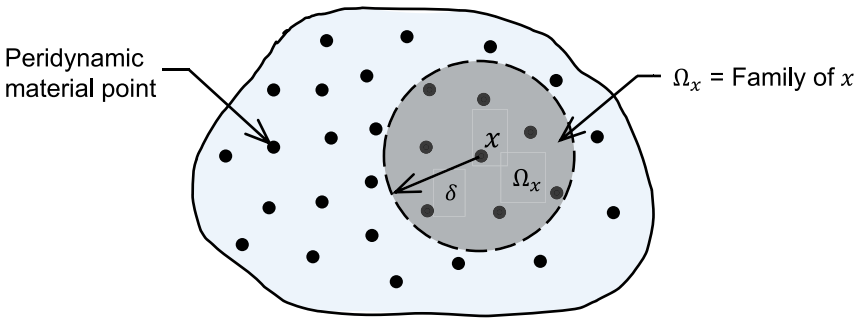

Fig. 1. Material points, family, and horizon in peridynamics.

the NDOs [31,59] are adopted. The NDOs approximate the gradient and divergence operators in the form of

$$\nabla \otimes \mathbf{A} = \int_{\Omega_x} \omega\langle\|\xi\|\rangle(\Delta \cdot \mathbf{A}) \otimes \left(\mathbf{K}_x^{-1}\xi\right) dV_{x'} \tag{8}$$

$$\nabla \cdot \mathbf{A} = \int_{\Omega_x} \omega\langle\|\xi\|\rangle(\Delta \cdot \mathbf{A}) \cdot (\mathbf{K}_x^{-1}\xi) dV_{x'} \tag{9}$$

$$\mathbf{K}_x = \int_{\Omega_x} \omega\langle\|\xi\|\rangle\xi \otimes \xi dV_{x'} \tag{10}$$

where $\mathbf{A}$ is an arbitrary scalar, vector, or tensor field, $\Delta \cdot \mathbf{A} = A_{x'} - A_x$ is the difference operator. $\mathbf{K}_x$ is defined as the shape tensor of material point $\boldsymbol{x}$. Substituting Eq. (8) into Eq. (7) yields the peridynamic form of volumetric flux as

$$\boldsymbol{q}(\boldsymbol{x},t) = -\frac{k}{\bar{\mu}} \int_{\Omega_x} \omega\langle\|\xi\|\rangle(\Delta \cdot \boldsymbol{\Phi}) \otimes (\mathbf{K}_x^{-1}\xi) dV_{x'} \tag{11}$$

Note that the derived volumetric flux equation directly takes the classical material intrinsic permeability as an input parameter, eliminating the need to find an equivalent micro-permeability as done in the bond-based PD. Applying the NDO expressed by Eqs. (9) to (6), the continuity equation of porous flow is obtained as

$$\frac{\partial}{\partial t}\left(\rho_f(\boldsymbol{x},t)\phi(\boldsymbol{x},t)\right) = -\rho_f \int_{\Omega_x} \omega\langle\|\xi\|\rangle(\Delta \cdot \boldsymbol{q}) \cdot (\mathbf{K}_x^{-1}\xi) dV_{x'} + R(\boldsymbol{x},t) \tag{12}$$

Solving Eq. (12) gives the updated pore fluid density in the porous medium which is used to calculate the hydraulic pressure via an Equation of State (EoS). The pore water pressure term is incorporated into the isotropic part of the scalar force state following [24,63] and the Eq. (3) is modified to the following form for poroelastic material:

$$t = \begin{cases} \dfrac{2((K - \frac{\mu}{3})\vartheta\langle\boldsymbol{x}\rangle + \alpha p)}{\bar{m}\langle\boldsymbol{x}\rangle}\omega\langle\|\xi\|\rangle\|\xi\| + \dfrac{8\mu}{\bar{m}\langle\boldsymbol{x}\rangle}\omega\langle\|\xi\|\rangle\underline{\mathrm{e}}^d & \text{for 2D.} \\ \dfrac{3(K\vartheta\langle\boldsymbol{x}\rangle + \alpha p)}{\bar{m}\langle\boldsymbol{x}\rangle}\omega\langle\|\xi\|\rangle\|\xi\| + \dfrac{15\mu}{\bar{m}\langle\boldsymbol{x}\rangle}\omega\langle\|\xi\|\rangle\underline{\mathrm{e}}^d & \text{for 3D,} \end{cases} \tag{13}$$

where α represents Biot's coefficient, which was introduced by Biot [69] as a supplement to the original effective stress principle. Biot's coefficient is defined as the ratio of the fluid volume change to the bulk volume change, and it controls the extent to which pore pressure contributes to the total stress in relation to the effective stress. α typically ranges from 0 to 1. p is the pore water pressure which is positive in compression. Tait's EoS [70] is adopted to compute pore water pressure in porous media and hydraulic pressure of fluid. The EoS is expressed by $p = \frac{K_f}{\gamma}[(\frac{\rho_f}{\rho_{f0}})^\gamma - 1] + p_b$ where K_f is the bulk modulus, ρ_{f0} and ρ_f are the initial and current fluid density, respectively, γ is a coefficient, p_b is the background pressure. In the subsequent simulations where water is modeled, the K_f has been taken as 22 MPa (note that it is taken much smaller than the bulk modulus for better numerical stability although it results in higher compressibility), γ is taken to be 7.5 and the background pressure is set to zero.

To consider the influence of deformation on porous flow, the porosity is updated by an iterative scheme following [24,71]:

$$\phi^{n+1}(\boldsymbol{x}) = \phi^n(\boldsymbol{x})(1 - C_r\Delta p) + \alpha(1 - \vartheta(\boldsymbol{x}))(C_r\Delta p + \Delta\vartheta(\boldsymbol{x})) + \frac{\Delta\rho_{Artificial}\phi^n(\boldsymbol{x})}{\rho_f(\boldsymbol{x},t)} \tag{14}$$

where n represents the time step, C_r denotes the compressibility of matrix material. Note that the formulation described above is a fully coupled hydro-mechanical formulation for poroelastic material where the mutual influence between the hydraulic field and mechanical deformation is incorporated. Note that the last term in Eq. (14) considers the influence of mass change caused by numerical stabilization algorithm (e.g., density smoothing) introduced in Section 2.5 on the porosity.

2.3. Damage model

To simulate crack initiation and propagation, the peridynamic bonds between material points are allowed to break. In this study, the critical stretch damage model [72,73] is adopted for modeling 2D brittle materials. The model assumes that a bond breaks irreversibly upon reaching a critical strain level given by

$$s_0 = \sqrt{\frac{G_c}{(4k' - 8\mu)\chi' + 8\mu\chi}} \tag{15}$$

where G_c represents critical energy release rate, k' is the two-dimensional bulk modulus, χ and χ' are the certain parameters of functions of the horizon size [74]. χ and χ' are set to 0.239δ and 0.804δ respectively, and $k' = E/[2(1-\upsilon)]$ for plane strain condition. For each peridynamic bond, a bond status variable g is defined as either 0 or 1, representing intact or broken status, respectively. At each material point, the damage $\tilde{\phi}$ is defined by

$$\tilde{\phi}(\boldsymbol{x}) = 1 - \frac{\int_{\Omega_x} g\langle\boldsymbol{\xi}\rangle dV_{\boldsymbol{x}'}}{\int_{\Omega_x} dV_{\boldsymbol{x}'}} \tag{16}$$

The definition of damage at material points explicitly quantifies the extent of damage and offers a straightforward index for monitoring initiation and propagation of cracks.

2.4. Semi-Lagrangian formulation for fluid

The classical PD theory is based on the total-Lagrangian formulation with an assumption of small deformation in the material. For modeling materials that experience large deformation (such as fluids), the semi-Lagrangian PD formulation [48–50,59,75], which is also referred to as Eulerian PD or updated Lagrangian formulation, was developed and proved effective. This formulation dynamically updates the neighborhood at each material point in response to material deformation, and the material response is assessed based on the current (i.e., deformed) configuration. As illustrated in Fig. 2, the neighborhood $B_{\boldsymbol{x}}$ of a peridynamic material point in semi-Lagrangian formulation does not change its shape with deformation. Instead, the neighboring points are updated at each time step. The equation of motion in the semi-Lagrangian PD is expressed by

$$\rho(\boldsymbol{x})\ddot{\boldsymbol{u}}(\boldsymbol{x},t) = \int_{B_{\boldsymbol{x}}} \left[\mathbf{T}(\boldsymbol{x},t)\langle\boldsymbol{x}'-\boldsymbol{x}\rangle - \mathbf{T}(\boldsymbol{x}',t)\langle\boldsymbol{x}-\boldsymbol{x}'\rangle\right] dV_{\boldsymbol{x}'} + \boldsymbol{b}(\boldsymbol{x},t) \tag{17}$$

which has a similar form to the total-Lagrangian PD except that the spatial range of integration is changed from $\Omega_{\boldsymbol{x}}$ to $B_{\boldsymbol{x}}$, indicating constant update of the neighborhood. The force state is computed referring to the non-ordinary form [31] as

$$\mathbf{T}(\boldsymbol{x},t)\langle\boldsymbol{x}'-\boldsymbol{x}\rangle = \omega\langle\|\mathbf{Y}\|\rangle\sigma_{\boldsymbol{x}}\mathbf{M}_{\boldsymbol{x}}^{-1}\mathbf{Y} \tag{18}$$

where $\sigma_{\boldsymbol{x}}$ represents the Cauchy stress tensor, $\mathbf{M}_{\boldsymbol{x}}$ denotes the shape tensor in the current configuration which should be updated at each time step by

$$\mathbf{M}_{\boldsymbol{x}} = \int_{B_{\boldsymbol{x}}} \omega\langle\|\mathbf{Y}\|\rangle\mathbf{Y}\otimes\mathbf{Y}dV_{\boldsymbol{x}'} \tag{19}$$

The Navier–Stokes equations are transformed into the following non-local integral form by using the NDO [59,60] and are solved at each material point:

$$\frac{D\rho}{Dt} = -\rho\int_{B_{\boldsymbol{x}}} \omega\langle\|\mathbf{Y}\|\rangle\boldsymbol{v}(\mathbf{Y})(\mathbf{M}_{\boldsymbol{x}}^{-1}\mathbf{Y})dV_{\boldsymbol{x}'} \tag{20}$$

$$\rho\frac{D\boldsymbol{v}}{Dt} = \int_{B_{\boldsymbol{x}}} \omega\langle\|\mathbf{Y}\|\rangle(\boldsymbol{\sigma}_{\boldsymbol{x}}\mathbf{M}_{\boldsymbol{x}}^{-1} + \boldsymbol{\sigma}_{\boldsymbol{x}'}\mathbf{M}_{\boldsymbol{x}'}^{-1})\mathbf{Y}dV_{\boldsymbol{x}'} + \mathbf{b}(\boldsymbol{x},t) \tag{21}$$

where $\boldsymbol{v}$ represents the velocity of a material point, $\boldsymbol{v}\langle Y\rangle$ denotes the relative velocity vector of a deformed bond. Solving the continuity equation Eq. (20) updates the density of fluid material points which can be used subsequently to calculate pressure. The Eq. (21) is equivalent to the equation of motion given in Eq. (17). To improve numerical stability of the fluid simulation, a density smoothing algorithm, together with artificial viscosity and particle shifting technique are used to mitigate the pressure oscillation and to prevent particle clustering issue [60]. These techniques are commonly used in smoothed particle hydrodynamics. For validation of the semi-Lagrangian PD approach in modeling fluids, a series of benchmark cases have been presented in an earlier work [60] where interested readers can refer to. Note that the formulations presented in this section are used for modeling free-flowing fluid and the flow in fractures. The flow inside the porous medium is handled by the poroelastic PD model as described in Section 2.2.

2.5. Fluid-solid interface

In the proposed computational scheme, the fluid outside porous media (including fluid in the fracture) is modeled by solving the Navier–Stokes equations in a semi-Lagrangian PD formulation, whereas the porous flow, which is governed by Darcy's law, is handled within the framework of a poroelastic PD formulation. It is therefore critical that a proper fluid-solid interface (FSI) model be developed to consider the leak-off of fluid into the porous medium. In other words, the mass exchange from the fluid inside the fracture towards the porous medium must be considered. In addition, the hydraulic pressure exerted by the fluid on the fracture

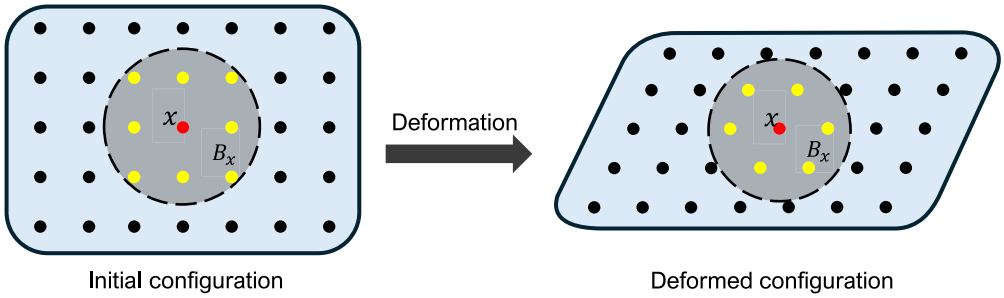

Fig. 2. Illustration of the neighborhood updating in semi-Lagrangian formulation.

surface must be accounted for in the FSI so that the propagation of fracture driven by the pressurized fluid can be captured. The FSI model proposed herein couples the semi-Lagrangion fluid model with the poroelastic model in PD. The model consists of two algorithms. One to quantify the interface forces between fluid and the poroelastic solid and the algorithm follows a previous work by Yang et al. [60]. The other one, which is first proposed in this work, accounts for the mass exchange between the fluid in the fracture and the porous flow (i.e., the leak-off process).

The FSI model is developed based on the concept of fictitious point. At each time step, the neighboring points of all fluid points are updated under the semi-Lagrangian scheme. If solid points are present within the neighborhood of a fluid point, that fluid point is identified as an FSI fluid point. This is illustrated in Fig. 3. The master point, which is a fluid point, has neighbors in both the fluid domain and the poroelastic solid domain. In this case, the solid neighboring points (i.e., the set B_s) are treated as fictitious fluid points. The forces between the master point and the fictitious fluid points (i.e., forces on bonds that cross the fluid-solid interface) can be conveniently calculated following the fluid model by

$$\mathbf{T}_i = \omega\langle\|\mathbf{Y}\|\rangle\boldsymbol{\sigma}_{\boldsymbol{x}}\mathbf{M}_{\boldsymbol{x}}^{-1}\mathbf{Y} \tag{22}$$

which is in the same form as Eq. (18). This interaction force is only calculated on the fluid material points and a reaction force with the same magnitude is applied on the neighboring solid points (i.e., fictitious fluid points). The shape tensor of fluid points at the interface, $\mathbf{M}_{\boldsymbol{x}}$, is constructed with the information of both the real fluid points and the fictitious fluid points, as expressed by

$$\mathbf{M}_{\boldsymbol{x}} = \int_{\tilde{\boldsymbol{B}}_s} \omega\langle\|\mathbf{Y}\|\rangle\mathbf{Y}\otimes\mathbf{Y}dV_{\boldsymbol{x}'} + \int_{\boldsymbol{B}_s} \omega\langle\|\mathbf{Y}\|\rangle(1-\tilde{\phi}_{\boldsymbol{x}'})\mathbf{Y}\otimes\mathbf{Y}dV_{\boldsymbol{x}'} \tag{23}$$

where B_s denotes the set of neighboring fictitious fluid points. When computing the fictitious point part of interaction force, the damage $\tilde{\phi}(\boldsymbol{x})$ at the solid point is considered to allow the fluid to enter the damaged solids. In addition, to prevent the fluid points' infiltration into the intact solids, a repulsive force $\boldsymbol{T}_r$ is implemented from only the immediate contact layer of the solids [60].

$$\mathbf{T}_r = -C_{RF}c_0^2 f(\eta)\left(1-\frac{\|\mathbf{Y}\|}{\Delta x}\right)\frac{\mathbf{Y}}{\|\mathbf{Y}\|^2} \tag{24}$$

where C_{RF} is a scaling factor that controls the magnitude of repulsive force to prevent unphysical penetration, c_0 represents the bulk wave speed, $f(\eta)$ is defined in the form of B-spline kernel function. The total force on a bond crossing the interface is the sum of $\boldsymbol{T}_i$ and $\boldsymbol{T}_r$, as expressed in Eqs. (22) and (24). The application of a repulsive force $\boldsymbol{T}_r$ also prevents overlapping between fluid points and completely damaged solid points. In the present study, the horizon at the FSI is chosen to be 2.5 times the element size. Note the horizon at FSI should be selected for the best performance of the FSI model. A too small horizon tends to cause intrusion of fluid material points into the solid domain, whereas a too large horizon imposes strong repulsion between the fluid points and adjacent solid points which may produce an unrealistic "gap" at the FSI. By experience, it is beneficial to select an FSI horizon consistent with the horizon used for solid and fluid. For the solid, a horizon of 2 to 3 times element size is commonly used with a balanced consideration between capturing crack branching and computational cost. For fluid, a horizon around 2 times element size is a common practice. In the present study, the horizons for both solid and fluid are set to be 2.5 times the element size and the same horizon is employed for the FSI model.

To model the leak-off occurring at the FSI, the fluid mass is allowed to transfer from fluid material points into the poroelastic solid. The outflowing volumetric flux on the fluid point is calculated based on the pressure gradient using the NDOs in the current configuration, as given by

$$\boldsymbol{q}(\boldsymbol{x},t) = -\frac{k}{\bar{\mu}}\int_{B_s}\omega\langle\|\mathbf{Y}\|\rangle(\boldsymbol{\Delta}\cdot p)\otimes(\mathbf{M}_{\boldsymbol{x}}^{-1}\mathbf{Y})dV_{\boldsymbol{x}'} \tag{25}$$

Eq. (25) is only applicable at the FSI on the fluid material points when they possess at least one neighboring point in the poroelastic medium. The leak-off is driven by the pressure gradient between the fluid points and the fictitious fluid points. The volumetric flux is computed with consideration of all neighbors including both the actual and fictitious fluid points. This helps to prevent obtaining irregular flow pattern due to lack of neighbors. In the equation, the intrinsic permeability k and dynamic viscosity $\bar{\mu}$ for the solid are adopted.

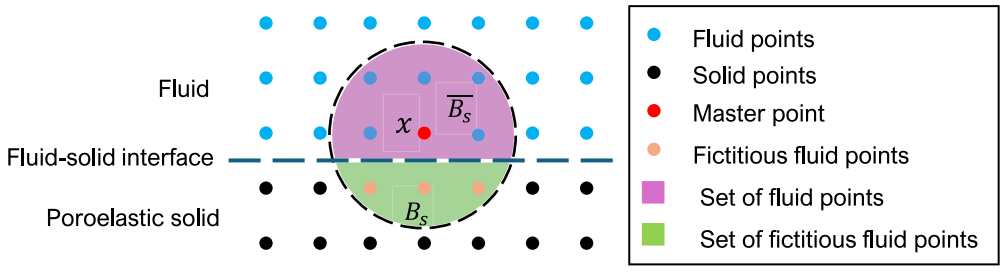

Fig. 3. Illustration of fluid-solid interface model.

The density change of a fluid point due to the leak-off is given by

$$\frac{\partial}{\partial t}\rho(\boldsymbol{x},t) = -\rho \int_{B_s} \omega\langle\|\mathbf{Y}\|\rangle(\Delta\cdot\boldsymbol{q})\cdot(\mathbf{M}_{\boldsymbol{x}}^{-1}\mathbf{Y})dV_{\boldsymbol{x}'} \tag{26}$$

It is slightly different from Eq. (12) as the current configuration is considered. Moreover, since the calculation is carried out on pure fluid phase, the porosity in Eq. (12) is set to a constant value of 1.0. The density change as calculated by Eq. (26) is further transformed into a mass change of the fluid point through:

$$\Delta m(\boldsymbol{x}) = \Delta\rho V_{\boldsymbol{x}} \tag{27}$$

where $\Delta m(\boldsymbol{x})$ denotes the mass change of fluid material point $\boldsymbol{x}$. Implementation of Eq. (26) also requires the shape function for the fictitious fluid points (i.e., poroelastic material points within the horizon of fluid points at the FSI). They are calculated by

$$\mathbf{M}_{\boldsymbol{x}} = \int_{\boldsymbol{B}_s} \omega\langle\|\boldsymbol{\xi}\|\rangle\boldsymbol{\xi}\otimes\boldsymbol{\xi}dV_{\boldsymbol{x}'} + \int_{\bar{\boldsymbol{B}}_s} \omega\langle\|\mathbf{Y}\|\rangle\mathbf{Y}\otimes\mathbf{Y}dV_{\boldsymbol{x}'} \tag{28}$$

where $\boldsymbol{B}_s$ and $\bar{\boldsymbol{B}}_s$ represent the set of solid point neighbor and fluid point neighbor, respectively. The shape function of fictitious points is obtained from two terms. The first term, which only involves the poroelastic material points, is calculated using the initial configuration. The second term, which involves the fluid points, is calculated using the current configuration and needs to be updated at each time step.

In the proposed FSI model, when the leak-off is prominent, the fluid material points are allowed to vanish when they lose all the mass they hold. To avoid potential numerical instability arising from large mass difference among the fluid material points, points that hold very small mass will be removed from the simulation with their mass re-distributed to neighboring points. In this study we set a threshold at 10% of the original mass of any material point, under which a fluid point will be removed and its mass is distributed to neighboring points by

$$\Delta m(\boldsymbol{x}') = m(\boldsymbol{x})\frac{\omega\langle\|\mathbf{Y}\|\rangle dV_{\boldsymbol{x}'}}{\int_{\bar{\boldsymbol{B}}_s}\omega\langle\|\mathbf{Y}\|\rangle dV_{\boldsymbol{x}'}} \tag{29}$$

where $\Delta m(\boldsymbol{x}')$ is the mass distributed to the neighboring point $\boldsymbol{x}'$ and $m(\boldsymbol{x})$ is the remaining mass of point $\boldsymbol{x}$ before its removal.

For the poroelastic material points at the FSI, in analogy to Eqs. (25) and (26), the flux equation and continuity equation possess the form of

$$\boldsymbol{q}(\boldsymbol{x},t) = -\frac{k}{\bar{\mu}}\left(\int_{\boldsymbol{B}_s}\omega\langle\|\boldsymbol{\xi}\|\rangle(\Delta\cdot\boldsymbol{\Phi})\otimes(M_{\boldsymbol{x}}^{-1}\boldsymbol{\xi})dV_{\boldsymbol{x}'} + \int_{\bar{\boldsymbol{B}}_s}\omega\langle\|\mathbf{Y}\|\rangle(\Delta\cdot p)\otimes(M_{\boldsymbol{x}}^{-1}\mathbf{Y})dV_{\boldsymbol{x}'}\right) \tag{30}$$

$$\frac{\partial}{\partial t}(\rho_f\phi) = -\rho_f\left(\int_{\boldsymbol{B}_s}\omega\langle\|\boldsymbol{\xi}\|\rangle(\Delta\cdot\boldsymbol{q})\cdot(M_{\boldsymbol{x}}^{-1}\boldsymbol{\xi})dV_{\boldsymbol{x}'} + \int_{\bar{\boldsymbol{B}}_s}\omega\langle\|\mathbf{Y}\|\rangle(\Delta\cdot\boldsymbol{q})\cdot(M_{\boldsymbol{x}}^{-1}\mathbf{Y})dV_{\boldsymbol{x}'}\right) \tag{31}$$

Note that the second term on the right hand side of Eq. (31) describes the rate of change in pore fluid density for poroelastic material points at the FSI. This terms indicates the fluid mass that is transferred from fluid to poroelastic medium. It shares the same form as the right hand side of Eq. (26) so that mass conservation is ensured when fluid flows into the porous medium.

2.6. Numerical stabilization and computational algorithm

NDOs are implemented in this research for gradient and divergence computation, which relying heavily on the shape tensor that is computed from the bond vectors linking each material point to its neighbors. The shape tensor is significantly impacted by its position within the material, particularly at the boundary compared to the interior. It may even be non-reversible if there are few neighbors within the horizon. This issue may lead to numerical error in the calculation for boundary particles [57,59,76]. The potential error may manifest as pressure oscillations because NDOs are used for the hydraulic part of the poroelastic model. To mitigate the pressure oscillations, a pore fluid density smoothing algorithm is utilized at the boundary, fracture surface and FSI in

the poroelastic medium. For a poroelastic solid point, its pore fluid density is smoothed by:

$$\rho_f(\boldsymbol{x},t)=\frac{\int_{\boldsymbol{B}_s}\omega\langle\|\boldsymbol{\xi}\|\rangle\rho_f(\boldsymbol{x}',t)dV_{\boldsymbol{x}'}+\int_{\bar{\boldsymbol{B}}_s}\omega\langle\|\boldsymbol{\xi}\|\rangle C\rho_f(\boldsymbol{x}',t)dV_{\boldsymbol{x}'}}{\int_{\boldsymbol{B}_s}\omega\langle\|\boldsymbol{\xi}\|\rangle dV_{\boldsymbol{x}'}+\int_{\bar{\boldsymbol{B}}_s}\omega\langle\|\boldsymbol{\xi}\|\rangle C dV_{\boldsymbol{x}'}} \tag{32}$$

where $\boldsymbol{B}_s$ and $\bar{\boldsymbol{B}}_s$ refer to the set of poroelastic neighbor point and fluid neighbor point, respectively, as illustrated in Fig. 3. ρ_f denotes the pore fluid density in the poroelastic medium or fluid density of the fluid material points. C is a coefficient which controls the weight of fluid points in the smoothing operation. The coefficient affects the rate of fluid infiltration into porous medium, independent of the material's permeability. By adjusting C, the interaction between fluid and poroelastic materials can be finely controlled to either dampen or enhance the infiltration. Making C sufficiently small minimizes the numerical effect on the infiltration process, which would be favorable for study of the transient response of fluid infiltration. Nonetheless, in scenarios where the permeability is low, achieving a steady state porous flow can be computationally demanding due to the inherent resistance of the poroelastic material to fluid infiltration. This often results in prolonged simulation time as the system slowly approaches equilibrium. Based on our experience, a unity value of C can significantly accelerate the establishment of a steady state porous flow and it has been adopted in the present study. It should be noted that applying Eq. (32) to the poroelastic material points at the FSI may in fact create or remove pore fluid mass. To ensure mass conservation, for any point $\boldsymbol{x}$, the pore fluid density change, $\Delta\rho_f(\boldsymbol{x},t)$, brought by the smoothing algorithm needs to be balanced by modifying the fluid density at its neighboring points. After obtaining the smoothed pore fluid density using Eq. (32), the corresponding increase/decrease in pore fluid mass at a point is compensated at its neighboring points for the purpose of fluid mass conservation.

The computational algorithm for modeling the fluid, porous medium, and coupling of the semi-Lagrangian and poroelastic PD formulations are summarized in "Algorithm".

Algorithm: Coupled semi-Lagrangian and poroelastic peridynamics algorithm

if $t=0$ **then**
  Initialize material points;
  Establish neighbor list and bonds in reference configuration;
  Compute shape tensor $\mathbf{K}$ for poroelastic points (10);
while $0<t$ *and* $t\le t_{end}$ **do**
  Update neighbor list and bonds in current configuration for fluid and FSI;
  Update velocity for half step, $\boldsymbol{v}^{n+1/2}=\boldsymbol{v}^n+1/2*dt*\boldsymbol{a}$;
  Update position to n+1 step: $\mathbf{Y}^{n+1}=\mathbf{X}_o+\mathbf{U}^n+dt*\boldsymbol{v}^{n+1/2}$;
  Implement bond damage $\tilde{\phi}$ and update bond status g (15), (16);
  Compute shape tensor $\mathbf{M}$ for fluid and fictitious fluid points (19), (23), (28);
  Compute volumetric flux $\boldsymbol{q}$ (7), (25), (30);
  Solve continuity equation for density change (12), (26), (31);
  Update fluid point mass m (27), pore pressure p (EoS), and porosity ϕ (14);
  Remove and redistribute small fluid particles (29);
  Activate fluid density smoothing (32);
  Solve Navier-Stokes equations (20), (21);
  Compute force state and FSI force(13), (18), (22), (24);
  Solve equation of motion (1), (17);
  Update velocity and acceleration to n+1 step;
  $t=t+\Delta t$, $n=n+1$;

3. Numerical simulations

In this section we present numerical simulations for validation of the proposed coupled fluid-poroelastic PD computational approach. First, a one-dimensional consolidation and a two-dimensional Mandel's problem are simulated for validation of the porous flow simulation and associated deformation. Then, simulation of a constant head test is presented to verify the accuracy of the FSI interface in terms of mass transfer from fluid to poroelastic domain. Lastly, simulations of hydraulic fracturing in porous medium are presented to demonstrate the capacity of the computational approach in capturing crack propagation with leak-off. The simulation results are compared with analytical solutions.

3.1. One-dimensional consolidation

The Terzaghi's one-dimensional (1-D) consolidation theory [77] has been widely used to predict how a saturated soil column consolidates over time. The 1-D consolidation problem assumes a constant load applied on a homogeneous soil column (i.e., a porous media). The excess pore water pressure generated by the load gradually dissipates with drainage of water from the upper end of the soil column, leading to volume reduction of the soil column. Here, we simulate the classical 1-D consolidation problem and compare the results with the analytical solution with respect to the dissipation process of excess pore water pressure and the corresponding

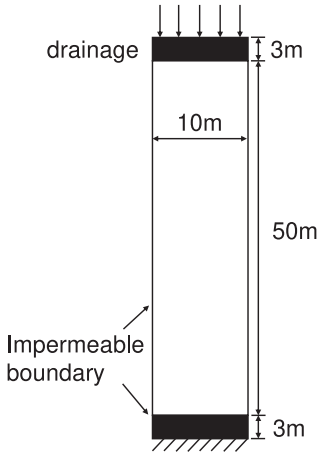

Fig. 4. 1D consolidation model.

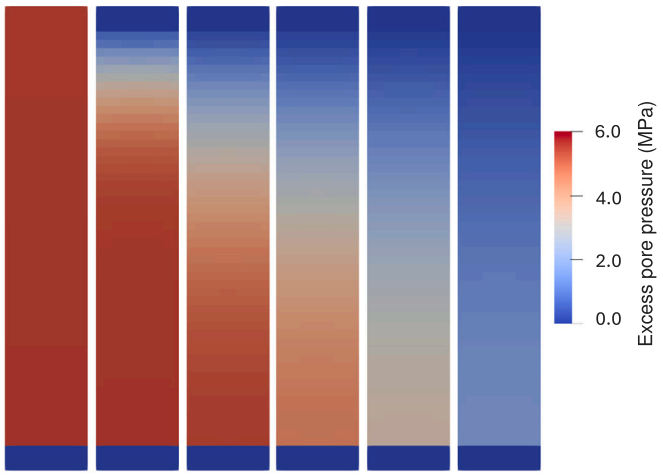

Fig. 5. Excess pore pressure distribution (left to right: time = 0, 1, 5, 10, 20, 40 s).

degree of consolidation. As shown in Fig. 4, the numerical model simulates a 50-meter-tall column of a poroelastic material, with a 3-meter thick fixed impermeable boundary at the bottom and a 3-meter thick drainage boundary at the top. Applying a finite thickness boundary layer is due to the difficulty of applying traction type boundary conditions in peridynamics and the thickness is selected to be the size of the horizon. The upper boundary layer is modeled with the same material points as for the column, whereas the lower impermeable boundary is modeled with the classical linear peridynamic solid model (i.e., no pore fluid involved), so that the model simulates a one-way drainage condition. The column is assumed to be fully saturated with water. A constant downward body force density is applied at the upper boundary as the external load, which induces a uniformly distributed initial excess pore water pressure of $p_0 = 6 \times 10^3$ kPa in the column before the start of drainage. For simplicity, gravity is not considered in the simulation. The intrinsic permeability, k, of the poroelastic material is set to 1.02×10^{-11} m^2, and the dynamic viscosity $\bar{\mu}$ of water is 1×10^{-3} Pa s. These correspond to a hydraulic conductivity $\bar{K}$ of 1×10^{-4} m/s in the porous medium. The bulk modulus and shear modulus of the porous material is 5 GPa and 4 GPa, respectively. The initial porosity of the column is set at 0.306.

After the external load is applied, the excess pore pressure gradually gets stabilized and uniformly distributed. In the present simulation, 10 s is found sufficient to reach a uniformly distributed excess pore pressure. The drainage boundary at the top is then activated where excess pore water pressure is fixed at zero. Assume the time to be zero when the drainage boundary is activated, the subsequent excess pore water pressure distribution at different times is obtained as shown in Fig. 5.

The analytical solution of the 1-D consolidation problem [77] is given by

$$p = \sum_{\hat{m}=0}^{\hat{m}=\infty} \left[\frac{2u_0}{M} \sin\left(\frac{Mz}{H}\right) \right] e^{-M^2 T_v} \tag{33}$$

where $\hat{m}$ is an integer and $M = \frac{\pi}{2}(2m+1)$, p_0 is the initial excess pore water pressure, z is depth, H is the total height of the column, T_v is the time factor. Eq. (33) gives the distribution of excess pore water pressure p at different times to quantitatively describe the

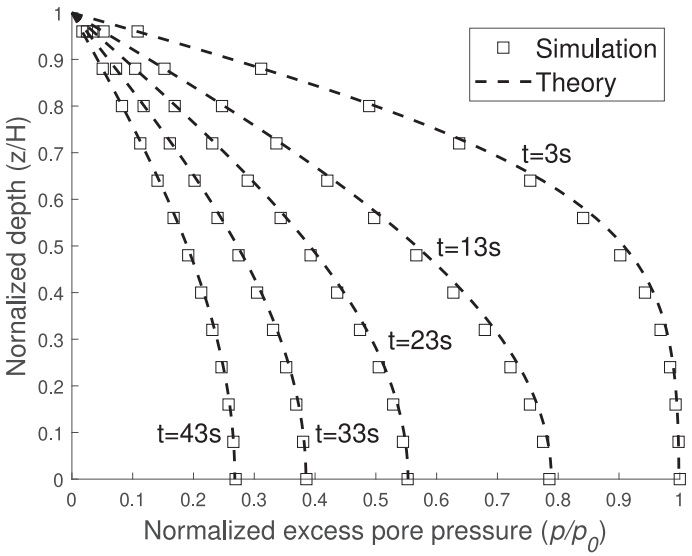

Fig. 6. Excess pore pressure profile along the column.

dissipation process. The degree of consolidation U, which represents the ratio of the vertical displacement at a given time to the final displacement, is expressed by

$$U_z = 1 - \sum_{\hat{m}=0}^{\hat{m}=\infty} \frac{2}{M} e^{-M^2 T_v} \tag{34}$$

Note that Terzaghi's 1-D consolidation theory assumes the solid and fluid to be incompressible. In order to compare the simulation results with the analytical solution, the elastic deformation of the poroelastic body obtained in numerical model, which occurs immediately after load application, is not taken into account in the subsequent comparisons.

A quantitative comparison of excess pore water pressure dissipation between the PD simulation results and theoretical solution is shown in Fig. 6. The depth is normalized by z/H where z refers to the vertical coordinate and H is the total height of the column. Similarly, the pore pressure is normalized by the initial pore pressure. The gradual dissipation of excess pore water pressure with time in the poroelastic material can be clearly observed. The simulation results align consistently with the theoretical solution at all times examined. Fig. 7 shows the degree of consolidation variation over time. Good agreement is observed between the simulation and the theoretical solution derived from classical 1-D consolidation theory.

3.2. Mandel's problem

The classical poroelasticity theory [69,78] assumes that a porous medium consists of both a porous solid phase and a pore fluid phase and they interact with each other. The theory enables modeling of solid medium deformation, pore fluid flow, and their interactions. The Terzaghi's consolidation theory used in the previous example assumes that both the solid and fluid phases are incompressible, focusing primarily on the change of pore space induced by external loading. In contrast, Biot's poroelasticity theory considers a linearly elastic, porous solid coupled with a slightly compressible viscous fluid. This provides a more comprehensive framework for assessing the consolidation processes. For a homogeneous and isotropic medium, the governing equation for the poroelasticity media [79] is expressed by

$$-(\lambda+\mu)\nabla(\nabla\cdot\boldsymbol{u}(x,t)) - \mu\boldsymbol{\Delta u}(x,t) + \alpha\nabla p(x,t) = \boldsymbol{f}(x,t) \tag{35}$$

where λ and μ are the Lamé constants, α is the Biot coefficient, $\boldsymbol{f}$ is the external force, $\boldsymbol{u}$ is the displacement, and p is the pore fluid pressure. The complexity of this differential equation makes it challenging to find general solutions, and thus, only a limited number of specific solutions are known. One such solution is Mandel's problem [80,81], which was initially applied to incompressible solids and fluids, focusing on pore pressure distribution. Mandel's problem was later extended to compressible materials, accompanied by a thorough investigation and a complete solution that provides analytical results for both displacement and stress [82,83]. Since Mandel's problem provides an easy fetching analytical solution for poroelasticity theory, it is considered suitable for validating poroelastic model [84–86].

Mandel's problem models a rectangular, fully saturated porous medium with unconfined permeable lateral boundaries on two sides, and is sandwiched by two rigid impermeable plates, as shown in Fig. 8. The model is assumed to have infinite length along the z-direction (perpendicular to the paper). If a vertical load of $2F$ (force per unit length in the z-direction) is applied to the upper

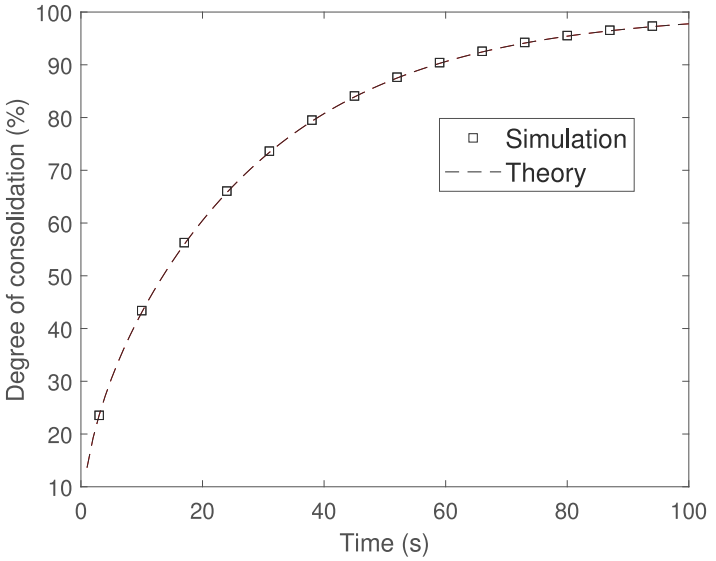

Fig. 7. Degree of consolidation over time.

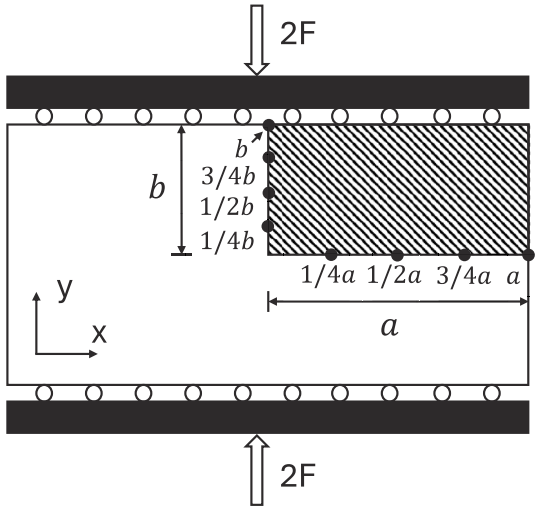

Fig. 8. Model of Mandel's problem with sampling location.

and lower boundaries, the initial excess pore water pressure p_0 and displacement $u_{x,0}$, $u_{y,0}$ induced by the vertical load are given by

$$p_0 = \frac{1}{3a}B(1+\upsilon_u)F \tag{36}$$

$$u_{x,0}(x) = \frac{F\upsilon_u x}{2\mu a} \tag{37}$$

$$u_{y,0}(y) = -\frac{F(1-\upsilon_u)y}{2\mu a} \tag{38}$$

where $B = \alpha M/K_u$ is the Skempton's coefficient, $\upsilon_u = \left[\frac{3\upsilon+\alpha B(1-2\upsilon)}{3-\alpha B(1-2\upsilon)}\right]$ is the undrained Poisson's ratio. $M = \left[\frac{\phi}{K_f} + \frac{\alpha-\phi}{K_s}\right]^{-1}$ is the Biot modulus, K_f and K_s are the bulk modulus of fluid and solid grain, respectively. $K_u = \lambda + \frac{2\mu}{3} + \alpha^2 M$ is the undrained bulk modulus, υ is the drained Poisson's ratio. The analytical solution for excess pore pressure dissipation and displacement history during the consolidation process are given by

$$p(x,t) = 2p_0 \sum_{n=1}^{\infty} \frac{\sin\beta_n}{\beta_n - \sin\beta_n\cos\beta_n}\left(\cos\frac{\beta_n x}{a} - \cos\beta_n\right)\exp\left(-\frac{\beta_n^2 ct}{a^2}\right) \tag{39}$$

Table 1
Parameters for Mandel's problem.

Parameter	Value	Parameter	Value
K_s (Pa)	1×10^{10}	α	1.0
K_f (Pa)	2×10^{9}	ϕ	0.3
λ (Pa)	4×10^{8}	$\bar{K}$ (m/s)	1×10^{-4}
μ (Pa)	4×10^{8}	ρ (kg/m^3)	1×10^{3}

$$u_y(y,t)=\left[-\frac{F(1-\upsilon)}{2\mu a}+\frac{F(1-\upsilon_u)}{\mu a}\sum_{n=1}^{\infty}\frac{\sin\beta_n\cos\beta_n}{\beta_n-\sin\beta_n\cos\beta_n}\exp\left(-\frac{\beta_n^2 ct}{a^2}\right)\right]y \tag{40}$$

where $c=\frac{\bar{K}}{\rho g(M^{-1}+\alpha^2 c_M)}$ is the consolidation coefficient, $\bar{K}$ is the hydraulic conductivity, $c_M=(\lambda+2\mu)^{-1}$ is the vertical uniaxial compressibility. β_n is the positive root of the nonlinear characteristic function given by

$$\tan\beta_n=\frac{1-\upsilon}{\upsilon_u-\upsilon}\beta_n \tag{41}$$

The Mandel's problem is modeled by the PD poroelastic formulation proposed in this paper. The model has a dimension $a\times b$ of 40×20 m. In view of the symmetry in Mandel's problem, only a quarter of the domain is considered in the simulation. Therefore, except for the right boundary, all other boundaries in the numerical model are impermeable. A vertical load of 1×10^4 N/m is applied at the upper and lower boundaries, compressing the porous medium. Material properties used in the simulation are summarized in Table 1.

The comparison between the simulation results and the theoretical solution is presented in Fig. 9. The pore pressure at four observation points located at 1/4, 1/2, 3/4, 1 of the distance a from the center $x=0$ (illustrated in Fig. 8), are plotted. The results generally indicate a decrease in pore pressure over time. Closer location to the drainage boundary is associated with faster pressure dissipation. The point at the drainage boundary does not possess excess pore pressure. The pore pressure in the analytical solution is observed to exceed the initial pore pressure p_0 immediately after load application and reduces afterwards. This non-monotonic behavior of pore pressure is known as the Mandel-Cryer effect [85,87], which is caused by the contraction of loading plate at the drainage boundary. The peak in the pore pressure is a transient phenomenon resulting from the communal effect of both mechanical and hydraulic behavior. The simulation results generally align well with the analytical solution and captures the Mandel-Cryer effect. However, the simulation results are seen slight deviated from the analytical solution. The error may potentially be attributed to the difference between the Mandel's problem and the setup of the numerical model. The original Mandel's problem consists of impermeable boundaries at top and bottom of the specimen with a smooth contact to the porous medium (refer to Fig. 8) whereas in the numerical model, the upper and lower boundary is modeled by a layer of material points with a finite thickness directly bonded with the material points in the porous medium. Another potential source of error may be associated with the numerical stabilization measures used in the simulation, which is believed to hinder the ability of the model to accurately capture transient response of material. The distribution of pore water pressure along the x-direction within the porous medium at different times is exhibited in Fig. 10 with comparison to the analytical solution. As expected, the pore pressure near the drainage boundary is observed lower compared to that in the center, and the pore pressure dissipates with time. The results from the PD simulation in general replicate the analytical solution for the behavior of porous flow. However, slight mismatch is evident at locations near the drainage boundary. This is likely a result of the numerical pressure oscillations and relevant numerical stabilization measures.

The vertical displacement at four sampling lines, located at 1/4, 1/2, 3/4, and the full distance b from the center $y=0$, is exhibited in Fig. 11. Given that the porous medium is linear elastic, the displacements of these four layers are proportional with their height from the bottom of the model. The displacement shows a decelerating trend. Good agreement is observed between the simulation results and analytical solution. The results demonstrates the capability of the PD model in accurately capturing the mechanical deformation of poroelastic solid subject to drainage of pore water.

Based on the Mandel's problem, convergence study of the proposed poroelastic model is performed under decreasing peridynamic horizon (δ-convergence) and under uniform grid refinement (m_{pd}-convergence). In the δ-convergence study, the effect of horizon δ is studied with fixed $m_{pd}=2$ and varied Δx of 0.5, 1.0, and 2.0 (unit: m), which yields $\delta=1.0$, 2.0, and 4.0, respectively, where $m_{pd}=\delta/\Delta x$ represents the ratio between horizon δ and discretized element size Δx. Fig. 12 presents the simulated excess pore water pressure dissipation history at $x=1/4a$ for $\delta=1,2$ and 4 with comparison to theoretical solution. Evidently, with reducing δ, the model can better capture the Mandel-Cryer effect, and the error in normalized pressure (i.e., the difference between theoretical solution and numerical result) is reduced. Then, the m_{pd}-convergence study is carried out with fixed $\delta=2.0$ while Δx is taken to be 0.5, 1.0, 2.0 (unit: m) with results shown in Fig. 13. Overall, the case with larger m_{pd} exhibits smaller error at the beginning and is better capable to capture the Mandel-Cryer effect. After sufficient time, the cases with $m_{pd}=2$ and $m_{pd}=4$ appear to have similar performance. The study confirms the δ-convergence and the m_{pd}-convergence of the model. An m_{pd} ranging between 2 to 4 is recommended under the consideration of both precision and computation demands.

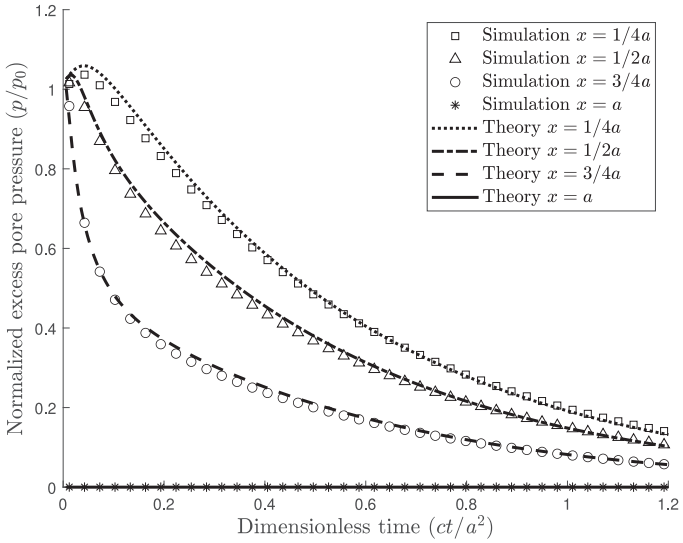

Fig. 9. Excess pore water pressure dissipation history.

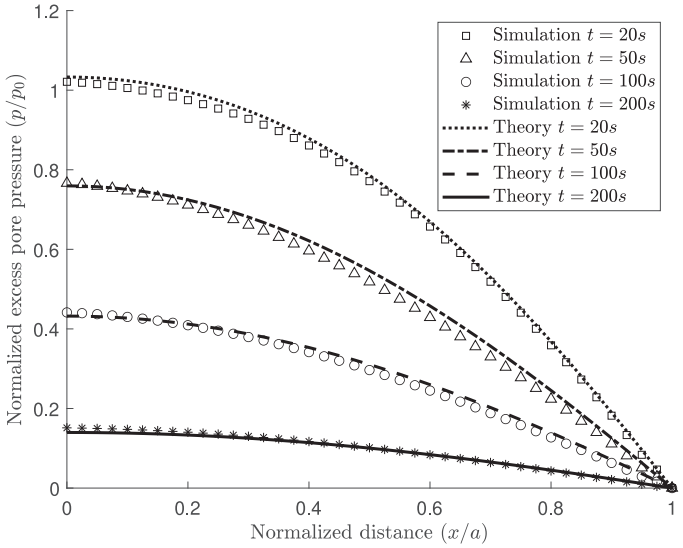

Fig. 10. Excess pore water pressure profile at selected times.

3.3. Constant head test

In this example, a simulation of the constant head test is carried out to validate the proposed fluid-solid interface (FSI) model. The FSI couples the semi-Langrangian PD formulation and the poroelastic PD model by allowing mass exchange from free-flowing fluid into porous flow. Constant head test [77] is a commonly used laboratory method to measure the permeability of coarse-grained soils with analytical solution available. In the test, water flow is enabled through a soil column subject to a constant head difference, and the total volume of water Q flowing through the soil specimen is given by

$$Q = A(\bar{K}\frac{h}{L})t \tag{42}$$

where A is the area of cross section of the soil specimen, t is the duration of test, L is length of specimen, $\bar{K}$ is the hydraulic conductivity, h is head difference. By measuring the flow volume and time, the permeability can be obtained from the above equation. To maintain the constant head difference, water tanks, which contains free flowing water, are often used at the upstream and downstream side of the specimen. The test therefore involves constant flow of water from the tank into the porous medium, which offers an opportunity to benchmark the proposed FSI model where the mass exchange between fluid and porous flow is simulated.

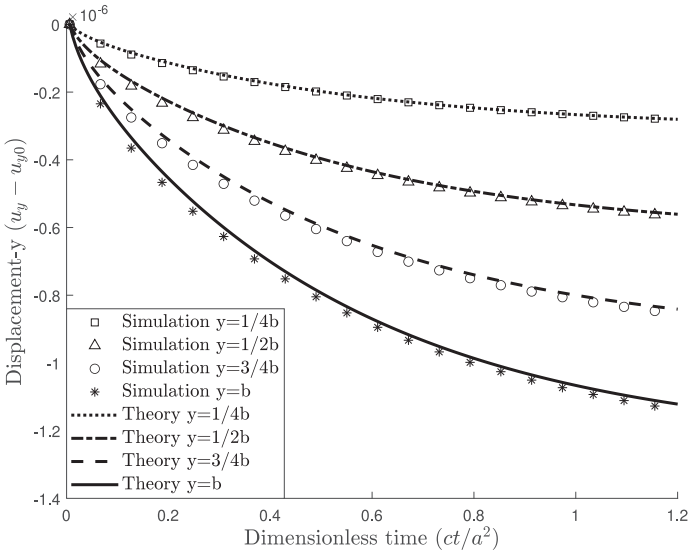

Fig. 11. Development of vertical displacement: comparison between simulation and theoretical solution.

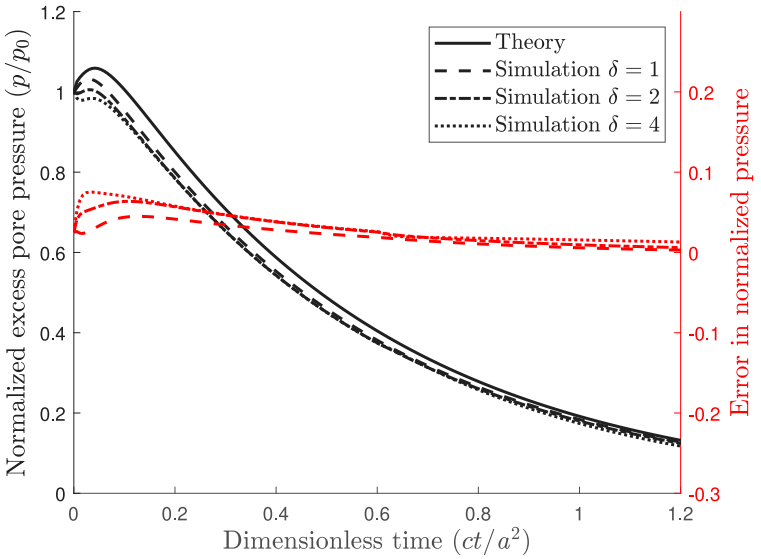

Fig. 12. δ-convergence: normalized excess pore pressure history at $x = 1/4a$ with varied δ.

For the purposes of the simulation, a simplified equivalent model of the constant head test is created as illustrated in Fig. 14 (left). The model consists of three material domains with two interfaces, namely, a dead weight block at the top, underlain by a domain of free flowing water which locates on top of the porous medium (i.e., the specimen). The bottom of the porous medium is modeled with a drainage boundary layer where the excess pore pressure is kept at zero. The dead weight block is modeled using the classical LPS model and interacts with the water underneath it via an ordinary FSI which couples the classical elastic PD model with the semi-Lagrangian PD model. A constant body force density of $\rho_w g$ is assigned to the dead weight block where ρ_w is water density and g is gravity constant. With a dead weight height of 10 m, an equivalent water head h of 10 m is being applied on the top of fluid. Note that the sole purpose of modeling a dead weight block is to create a constant pressure inside the water which is equivalent to a constant head difference in the porous medium. Gravity is not considered in the simulation. The interface between the water and the porous medium is critical as it simulates the process that free water enters porous flow. This serves the primary focus of this simulation. The porous medium and the drainage boundary layer are fixed in both x and y directions, while the dead weight block and the water are allowed to move along the y direction and are fixed in x direction.

In the simulation, hydraulic conductivity of the porous media $\bar{K}$ is 1×10^{-4} m/s, length of the porous medium L is 50 m, and the width of the specimen is 20 m. As shown in Fig. 14 (middle), the pore pressure uniformly decreases along the vertical direction from

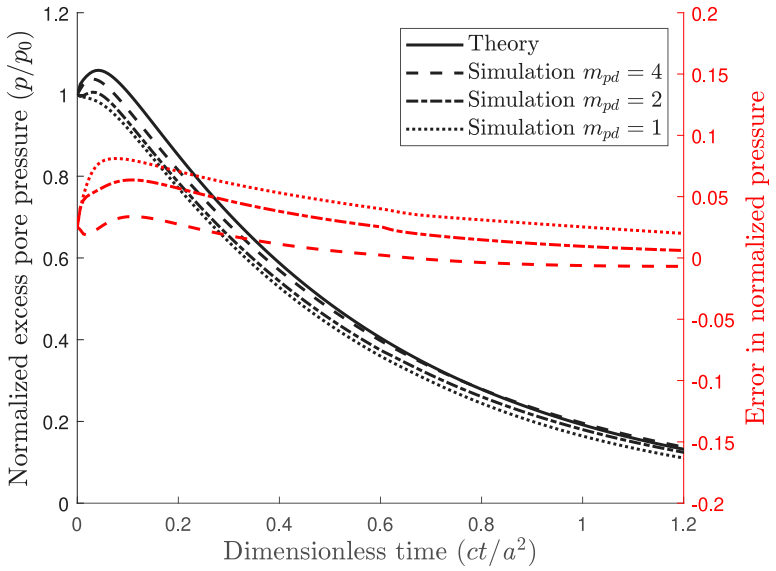

Fig. 13. m_{pd}-convergence: normalized excess pore pressure history at $x = 1/4a$ with varied m_{pd}.

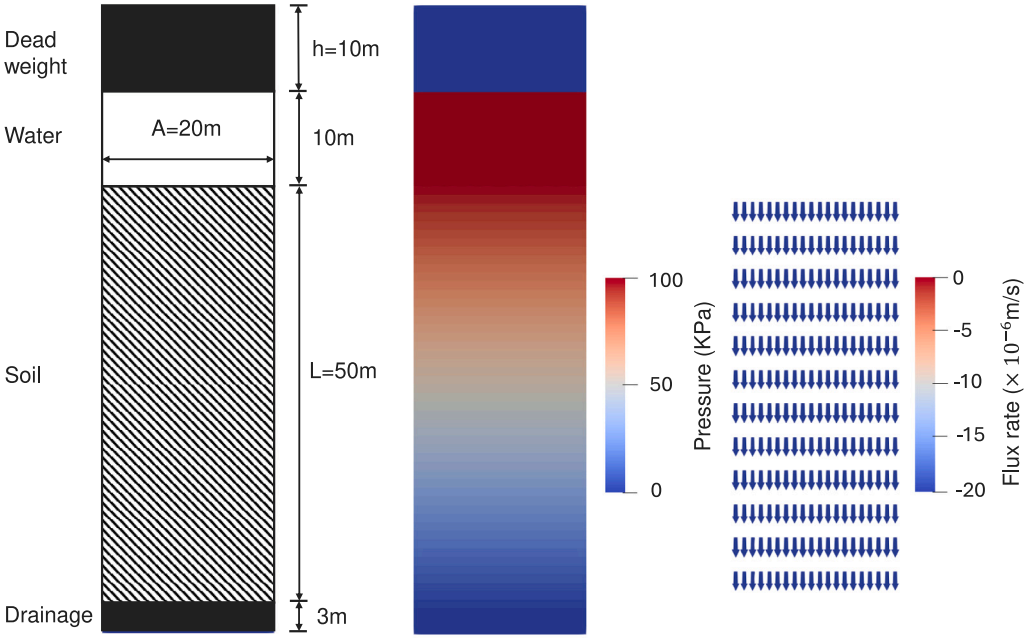

Fig. 14. Constant head test model (left), simulated pressure distribution (middle), simulated flux distribution (right).

a maximum 10-m water head to zero. A stable volumetric flux rate $q = \bar{K}i = 2 \times 10^{-5}$ m/s is observed in the porous medium as shown in Fig. 14 (right). Note that the density smoothing algorithm expressed in Eq. (32) is necessary to produce stable flow flux crossing the fluid-poroelastic solid interface and near the drainage boundary. Otherwise the flux can be ill-posed at the interface/boundary since there is no pressure difference within the free flowing fluid or drainage boundary layer. The coefficient C in Eq. (32) is suggested to be 1.0 for the best performance. Fig. 15 shows the water flow volume through the simulated specimen. This volume is obtained by monitoring the loss of fluid mass in the fluid material points at the FSI and assuming a constant density for water. As expected, the flow volume increases with time which is consist with the theoretical result calculated using Eq. (42). Also, the pressure in the fluid domain is kept constant during the simulation by applying the dead weight. The above simulation of the constant head test demonstrates the effectiveness of the proposed FSI in capturing the mass exchange from the free fluid into the porous flow.

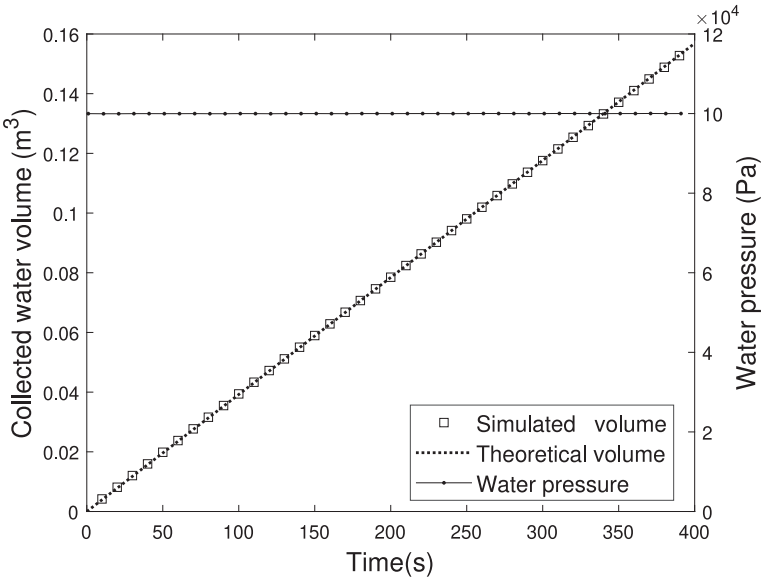

Fig. 15. The time variation of volume of water flowed through the specimen and pressure of water above the specimen.

3.4. Hydraulic fracturing in porous medium

A series of simulations are carried out to test the ability of the proposed computational approach in modeling hydraulic fracture propagation in porous medium with concurrent consideration of leak-off effect. The simulations are validated with the Kristianovich-Geertsma-de Klerk (KGD) [88] model for plane strain hydraulic fracturing in conjunction with the Carter's equation [89] which models the fluid leak-off dynamics. The KGD model is a classical model offering analytical solutions for fluid-driven crack propagation. It assumes an infinite elastic brittle solid characterized by Young's modulus E, Poisson's ratio υ, toughness K_{IC}, intrinsic permeability k, porosity ϕ, and fracturing fluid with viscosity $\bar{\mu}$, while the gravity effect is not considered. The fracturing fluid is injected with a constant volumetric flow rate Q_0 into the solid, which generates a radially symmetric fracture. Carter's equation provides an analytical solution to 1D fluid flow leak-off into porous media, assuming Darcy's law is applicable to the porous flow. The Carter's leak-off velocity v_L and leak-off coefficient C_L [90] are given by:

$$v_L = \frac{C_L}{\sqrt{t - t_0}} \tag{43}$$

$$C_L = \Delta p \sqrt{\frac{k\phi C_t}{\bar{\mu}\pi}} \tag{44}$$

where Δp is the pressure drop from the surface of fracture to a remote location, and C_t is the total compressibility of the porous medium.

A plane-strain hydraulic fracturing problem is simulated as illustrated in Fig. 16. The fracture propagation is assumed to be toughness-dominated, meaning that the fluid's viscosity induced energy dissipation is negligible and the fracturing is governed by the toughness of the solid. The analytical solution for toughness-dominated hydraulic fracturing with leak-off is given in [91] which combines the classical KGD solution with the Carter's equation. The solution for crack length l is given by:

$$l = \begin{cases} 2\left(\frac{E'Q_0}{\pi K'}\right)^{\frac{2}{3}} t^{\frac{2}{3}} & \frac{E'^4 C'^6}{K'^4 Q_0^2} t \ll 1 \\ \frac{Q_0}{\pi C'} t^{\frac{1}{2}} & \frac{E'^4 C'^6}{K'^4 Q_0^2} t \gg 1 \end{cases} \tag{45}$$

where $E' = \frac{E}{1-\upsilon^2}$, $K' = 4\left(\frac{2}{\pi}\right)^{\frac{1}{2}} K_{IC}$, and $C' = 2C_L$. In Eq. (45), the first equation corresponds to a storage-dominated regime, where leak-off is assumed to have negligible effect on crack development (i.e., with a relatively small permeability of the porous medium, the fracture extends with limited leak-off). The second one correspond to a leak-off dominated regime where the toughness is small. Correspondingly, two simulations are carried out, one for the storage-dominated scenario and one for leak-off dominated scenario. The simulation results are compared with the above analytical solutions.

The setup of the numerical model is illustrated in Fig. 17. The porous solid is created with a dimension of 150 mm by 200 mm with an existing crack at the top boundary where fluid is injected in. The existing crack has a depth of 10 mm and a width of 4 mm. The fluid particles are pushed towards the crack with a constant injection rate. The size of material points in this model is

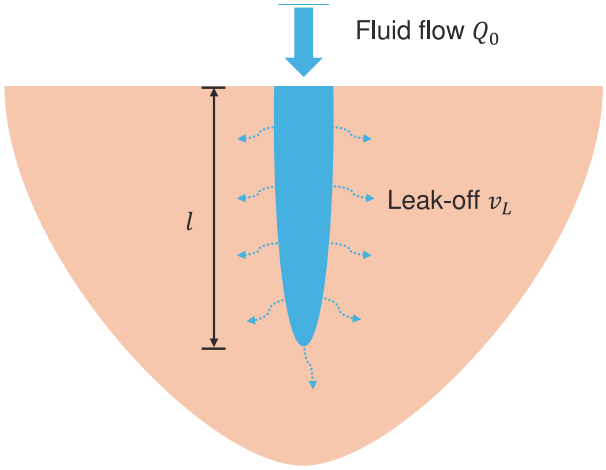

Fig. 16. Illustration of plane strain hydraulic fracturing problem with leak-off.

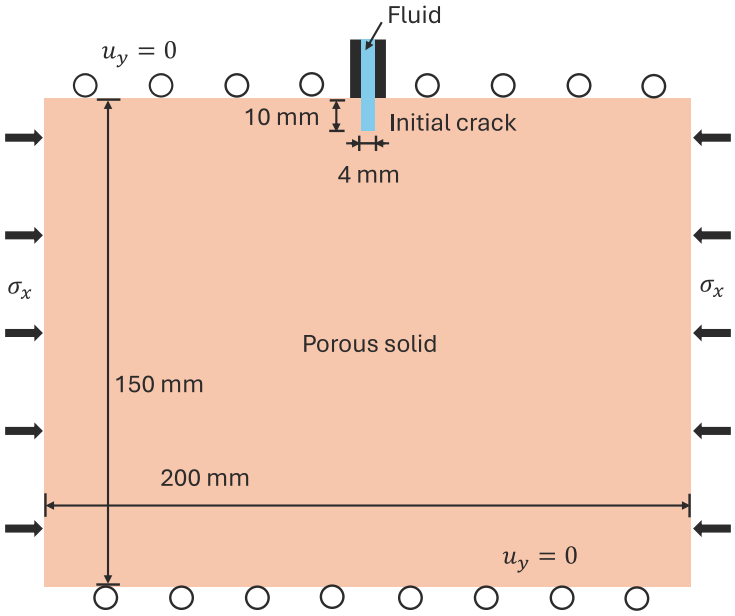

Fig. 17. Setup of hydraulic fracturing model.

Table 2
Parameters for porous solid.

Parameter	Value	Parameter	Value
Young's modulus E (MPa)	700	Density (kg/m^3)	1.61
Poisson's ratio υ	0.25	Initial porosity	0.1
Permeability k (mm^2)	1.02×10^{-9}	Energy release rate G_c (MPa mm)	0.005

set to 1 mm. The porous solid is modeled with poroelastic PD formulation while the injected fluid is modeled with material points governed by the semi-Lagrangian PD formulation with Tait equation of state.

For the storage-dominated case, the injection rate of fluid is set to of 0.16 mm^3/ms and the lateral confining pressure is 0.21 MPa. Similar to the models presented in earlier sections, the confining pressure is applied to a boundary layer in the form of a body force density. The boundary layer is set with a thickness of the size of horizon. Material parameters used for the porous solid are summarized in Table 2. For the fluid, an initial density of 1×10^3 kg/m^3 and viscosity at 1 MPa s are adopted. The horizon of all the particles, including those at FSI, is 2.5 times of particle size.

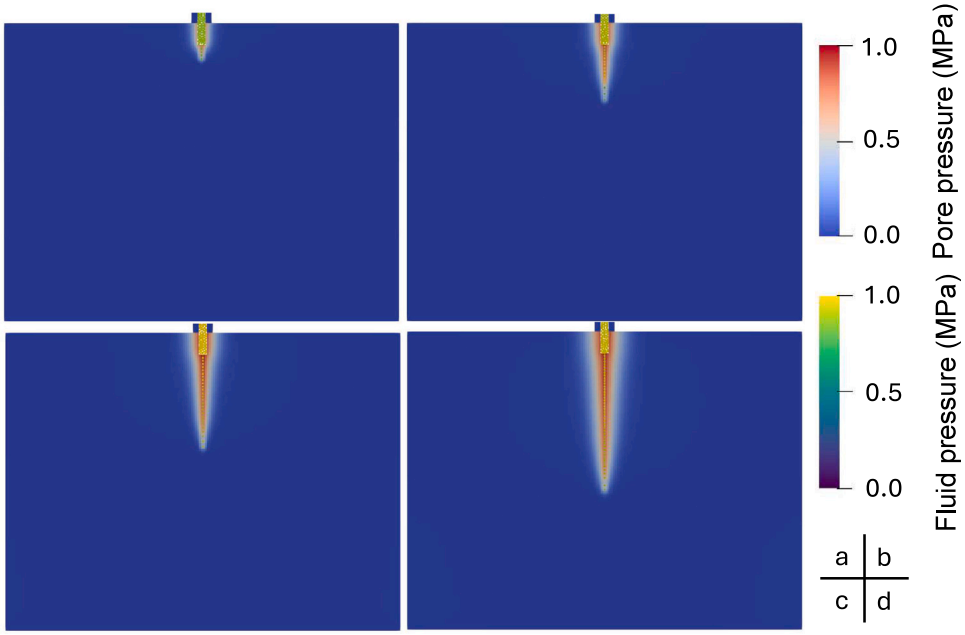

Fig. 18. Simulated fluid pressure distribution at 5 ms (a), 25 ms (b), 50 ms (c) and 100 ms (d) for the storage-dominated case.

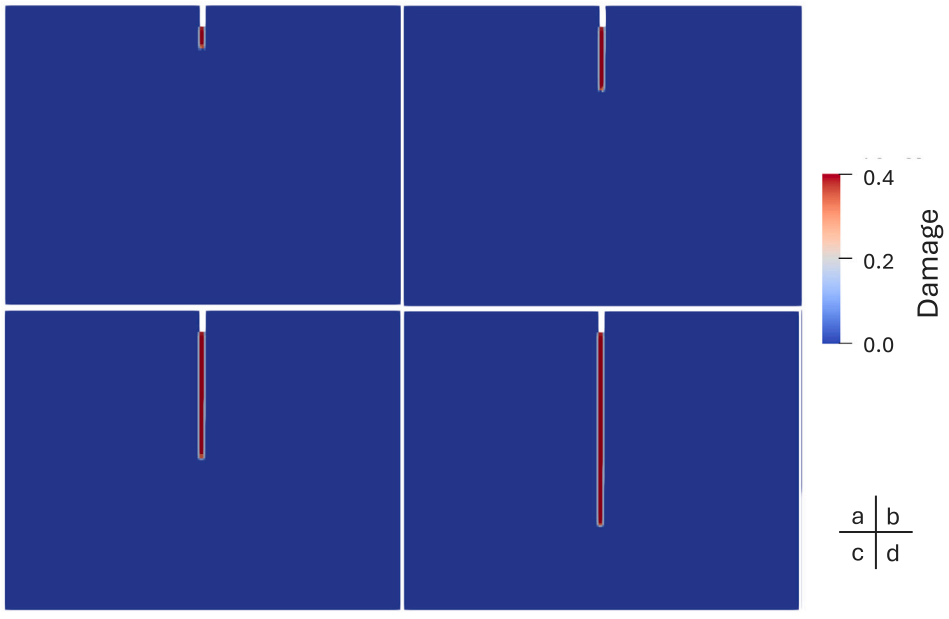

Fig. 19. Damage progress at 5 ms (a), 25 ms (b), 50 ms (c) and 100 ms (d) for the storage-dominated case.

The fluid is injected into the existing crack from an uncompressed state, and its pressure increases until the crack begins to propagate. The distributions of fluid pressure inside the crack and pore pressure in the porous medium at 5 ms, 25 ms, 50 ms, and 100 ms after the beginning of crack propagation are shown in Fig. 18. The simulation reveals several common phenomena observed in hydraulic fracturing. Notably, there is a lag between the fluid front and the fracture tip, with the pressure at the fluid front being lower than the injection pressure. During the hydraulic fracturing process, the fluid continuously infiltrates into the surrounding porous solids. However, due to the low permeability of the porous solid, the infiltration is limited to the vicinity of the crack. As fluid injection continues, the crack propagates in the vertical direction, corresponding to the direction of minimum principal stress, as exhibited in Fig. 19.

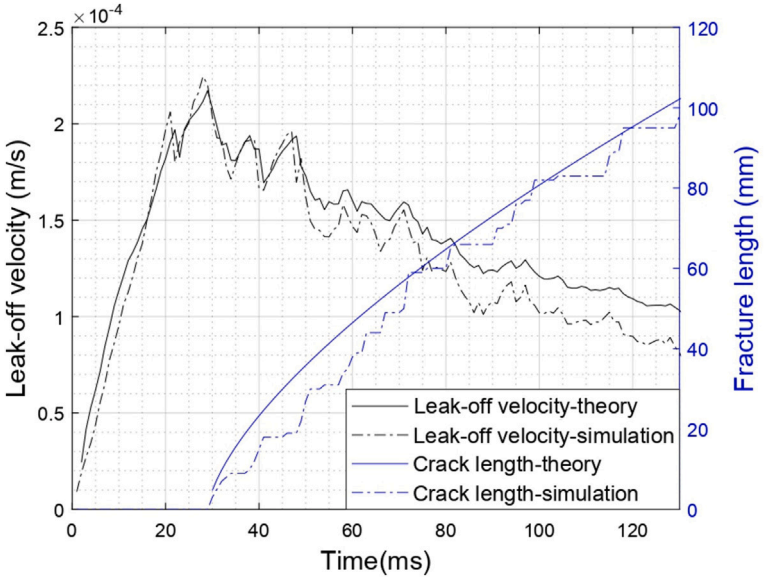

Fig. 20. Average leak-off velocity variation and fracture extension over time for the storage-dominated case.

The Carter's leak-off velocity is calculated using Eq. (43) and is used for comparison with numerical simulation results. As the leak-off velocity is pressure-dependent, the average fluid pressure inside the crack is used for obtaining the analytical solution. In the numerical simulation, the leak-off velocity is calculated by dividing the leak-off volumetric rate by twice the wet fracture length. The result is therefore an average leak-off velocity at the fracture. In each calculation step, the leak-off volumetric rate is obtained by dividing the mass reduction in the fracturing fluid by the fluid density and time step size. A comparison of the analytical solution and the simulation result with respect to the average leak-off velocity is shown in Fig. 20, where reasonable agreement is seen. For the purpose of comparison, the artificial mass transfer resulted from the density smoothing algorithm is disregarded. Note that such artificial effect can be effectively mitigated by taking a small value of the coefficient C in Eq. (32). The fluctuations in the leak-off velocity are resulted from varying fluid pressure and are more apparent in the early stage of fracturing. The drops in the leak-off velocity implies pressure reduction in the fluid. This is believed to be caused by the movement of fluid material points into the fractured zone when fracture advances. It should be noted that such effect may be dependent of the element size used for modeling fluid. Adopting relatively small fluid element size (relative to the aperture of the fracture) may mitigate such effect and render a less fluctuating response of the leak-off velocity.

The extension of fracture length is plotted in Fig. 20 with reference to the right axis. The fracture length refers to the distance between the bottom of the initial crack and the tip of fracture (herein defined as the furthest point with damage exceeding 0.4). Evidently, the fracture extension begins at 28 ms after injection. The simulated fracturing process is characterized by the alternating stages of fracture growth and stress build-up. The growth of fracture is compared with the analytical solution derived from Eq. (45). Note that the value of $\frac{E'^4 C'^6}{K'^4 Q_0^2}$ is on the order of 10^{-4}, indicating that storage effects dominates and the leak-off is relatively small. Therefore, the solution corresponds to the storage-dominated regime is utilized for comparison. The simulation results align closely with the analytical solution, with slightly slower fracture propagation possibly due to the effect of the limited leak-off.

Fig. 20 also illustrates the interplay between leak-off velocity and crack propagation. The leak-off velocity is believed to be influenced by two competing mechanisms - the injection induced pressure rise and the pressure release due to fracture extension. In early stage of fracturing, both effects are apparent. In the fracture extension curve, when stress builds up (e.g., characterized by the flat part of the curve between fracture extension events), the fracture does not grow and hydraulic pressure is accumulated in the fracture which is implied by the increasing leak-off velocity. The fracture grows when the damage criterion is satisfied, and this process is accompanied by the hydraulic pressure release and reduction in leak-off velocity. In a later stage of fracturing (e.g., after 60 ms) when the fracture has extended for some distance, the stress build-up stage is no longer associated with apparent accumulation of hydraulic pressure, and the leak-off velocity shows a continues dropping trend. The behavior is different from the early stage of fracturing, possibly because the injection-induced hydraulic pressure becomes much lower than that in the early stage of fracturing [60].

As a verification of the fluid mass conservation property of the presented formulation, the variations of the pore fluid mass and fracturing fluid mass throughout the simulation are shown in Fig. 21. The pore fluid mass increases continuously during the simulation, while the mass of the fracturing fluid decreases accordingly during leak-off. The total fluid mass in the simulation (i.e., the sum of the fracturing fluid and pore fluid), remains constant which verifies that the proposed formulation well maintains fluid mass conservation.

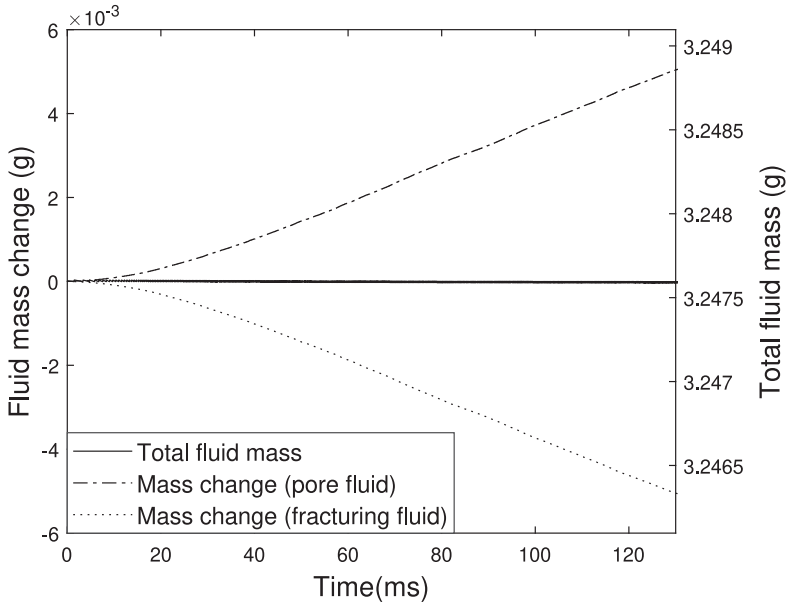

Fig. 21. Mass exchange between fluid and porous media.

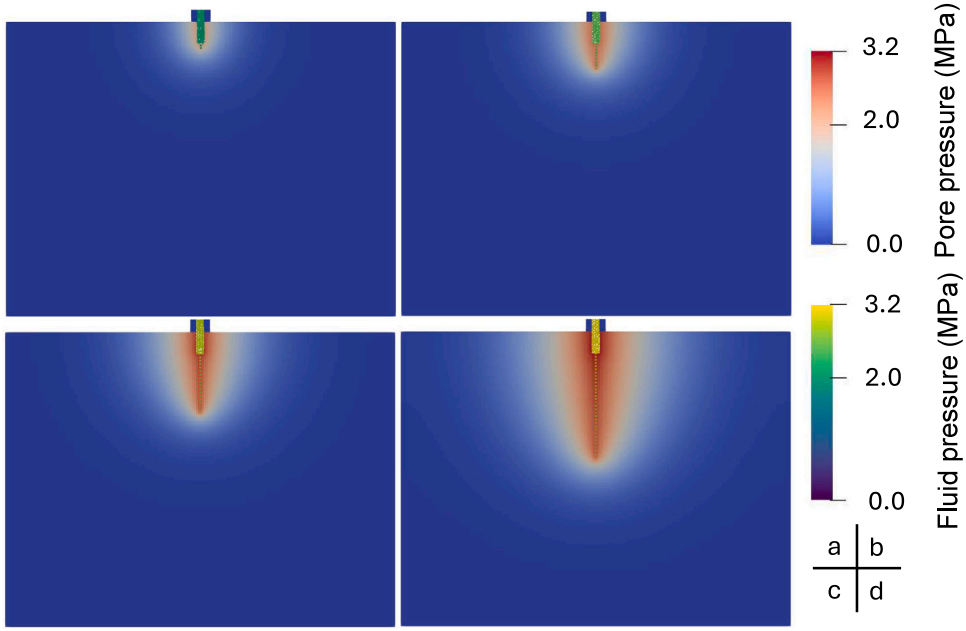

Fig. 22. Simulated fluid pressure distribution at 5 ms (a), 25 ms (b), 50 ms (c) and 100 ms (d) for the leak-off dominated case.

The second case simulates the hydraulic fracturing under a leak-off dominated condition. Material properties and model settings are adjusted to ensure the leak-off domination. For the porous solid, the Young's modulus is 4000 MPa, energy release rate is 0.002 MPa·m, and the permeability is 1.02×10^{-8} mm^2. The injection rate is set to 0.08 mm^3/s for this simulation. For the purpose of validation with analytical solution, a lateral confining pressure of 0.9 MPa is applied on the left and right boundaries to minimize the fluid lag. Note that confining pressure commonly exists in underground stress conditions. Hydraulic fracturing of a brittle material without any confining pressure could develop in a rather fast manner with a large lag between fluid front and crack tip, which is not the purpose of the present simulation. After crack initiation, the value of $\frac{E'^4 C'^6}{K'^4 Q_0^2}$ is on the order of 10^2, indicating the dominance of the leak-off effect. The pressure distribution in the fracture and the porous medium throughout the simulation is shown in Fig. 22. The pressurized fluid infiltrates into the surrounding porous media and permeates to a much broader area compared to the previous

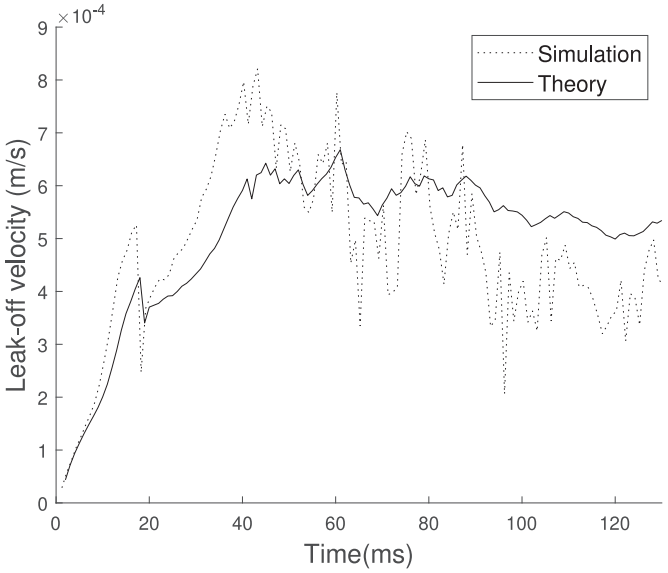

Fig. 23. Variation of average leak-off velocity in the leak-off dominated case.

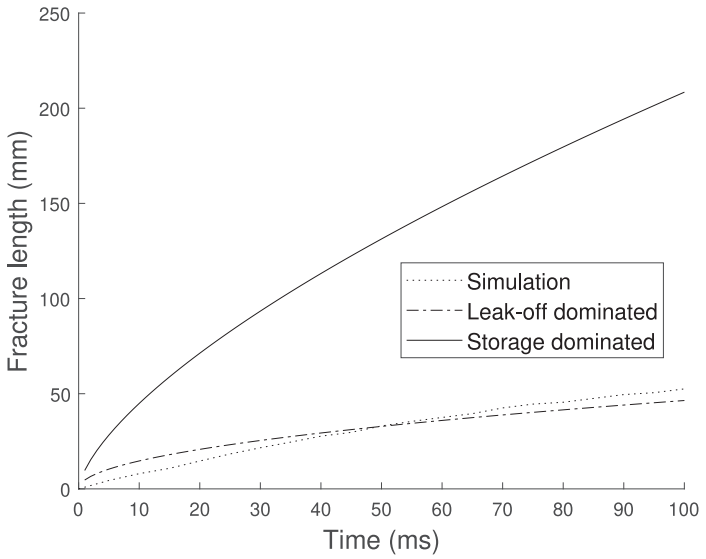

Fig. 24. Fracture growth in leak-off dominated case and comparison with analytical solution.

simulation. The injection-induced fracture propagates in the vertical direction, however, at a slower rate compared to the toughness-dominated case. This is expected since the leak-off leads to loss of fluid inside the fracture which tends to reduce the fluid pressure and creates an unfavored condition for fracture propagation.

The obtained leak-off velocity is shown in Fig. 23 with comparison to the solution of Carter's equation. The fluid pressure fluctuates as the crack propagates, this can be possibly attributed to the brittle nature of the porous solid which brings dynamic effect when fracture develops. Overall, the simulation results align with the analytical solution. In Fig. 24, the fracture length is plotted and compared with the analytical predictions for both storage dominated and leak-off-dominated conditions. As the pressurized fluid constantly leaks into the surrounding porous media, the fracture develops apparently slower than the analytical solution for the storage-dominated case. Nevertheless, the simulation results are consistent with the leak-off dominated solution. For simulation of hydraulic fracturing in high-permeability solid media, the consideration of leak-off in the simulation is therefore indispensable, as the storage-dominated model will largely overestimate the fracture propagation. The above two simulations provide a quantitative validation of the proposed computational approach for modeling fracture propagation in porous medium under both storage-dominated and leak-off-dominated conditions.

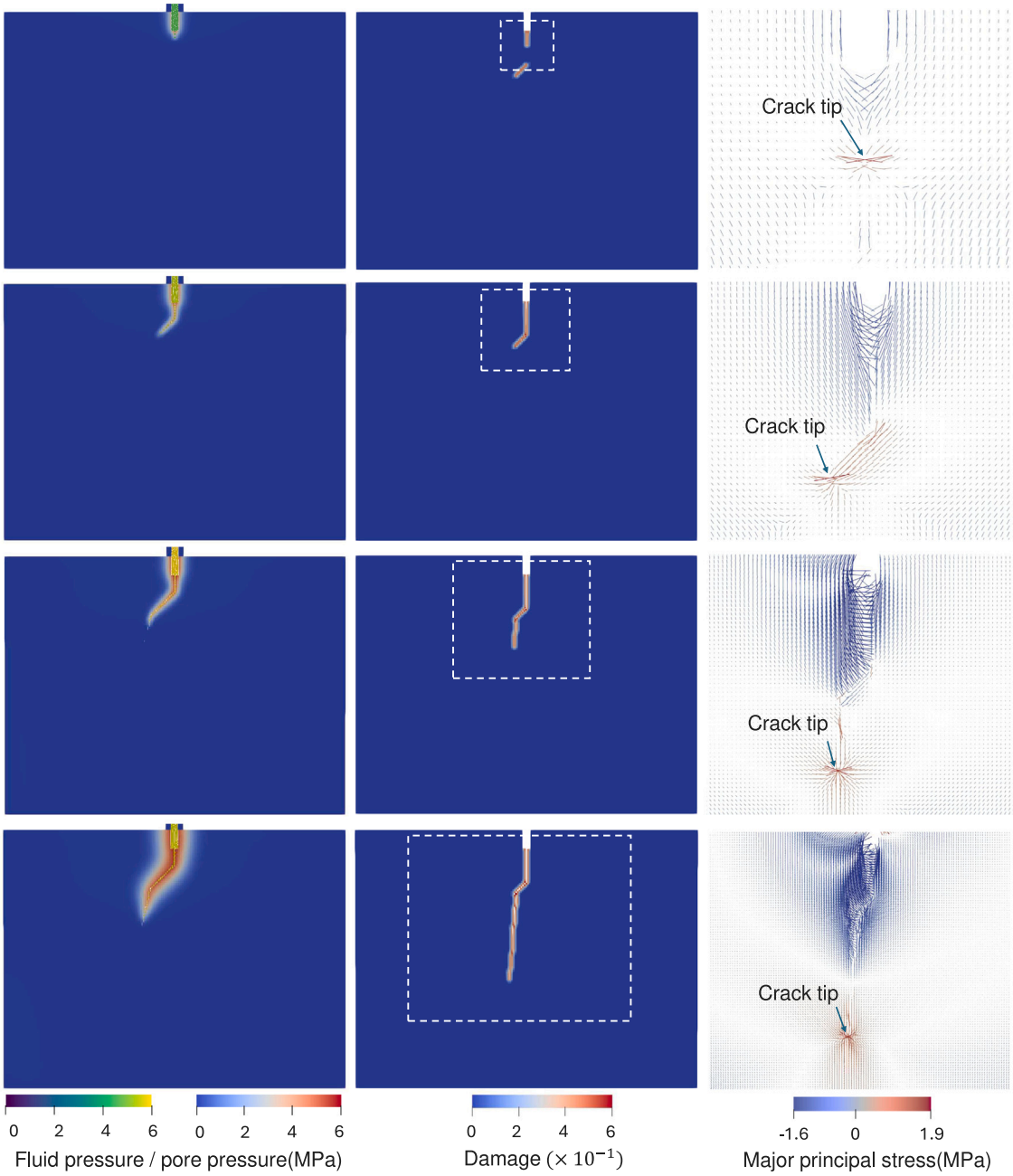

Fig. 25. Pressure, damage, and major principal stress distribution during fracturing (from top to bottom: time = 5, 17, 29, 141 ms). The location of the domain shown in the right column is indicated by the dashed line in the middle column. (For interpretation of the references to color in this figure legend, the reader is referred to the web version of this article.)

In the last example, we showcase the simulation of fracture development in conjunction with a pre-existing natural crack. The natural crack is positioned 20 mm below the initial crack, measuring 10 mm in length and inclined at 45 degrees towards the lower left. All bonds along this natural crack are initially set to broken. The poroelastic material parameters and loading conditions match those in the storage-dominated case, but the lateral confining pressure is set to 1.5 MPa to minimize the fluid lag. The evolution of the hydraulic pressure, fracture, and major principal stress field are shown in Fig. 25. In the third column of the figure, the colored line segments indicate the direction of major principal stress, with colors representing its magnitude and positive values for tension. The fracture is found propagating perpendicular to the major principal stress direction (i.e., mode I) near the tip. The hydraulic fracture grows and connects with the natural crack, followed by infiltration of fluid into the natural fracture. As fluid injection

continues, the fracture continues to propagate downward due to the horizontal tensile stress. In this case, the fracture propagates along a path slightly deviates from the vertical direction, possibly due to the influence of the existing fracture. Further study and validation on hydraulic fracturing with more complex configuration of pre-existing natural fractures is beyond the scope of current study, as contact at the fractured surfaces may play a more significant role and should be addressed with care.

4. Conclusions and discussions

This paper introduces a unified PD-based computational approach for modeling hydraulic fracturing in poroelastic medium with consideration of the leak-off effect. The injected fluid is simulated by a semi-Lagrangian formulation of PD and the porous medium is modeled by a non-local poroelastic PD formulation. The porous flow equation suited for state-based peridynamics is derived based on the non-local differential operator and Darcy's law. A novel FSI model is proposed to couple the semi-Lagrangian and poroelastic models of PD. The proposed computational approach is first validated with the 1-D Terzaghi consolidation problem and the 2-D Mandel's problem for its capacity in modeling porous flow and mechanical deformations. Simulation is further carried out for a constant-head test to validate the FSI model especially for its capacity in modeling fluid mass exchange between fluid in the fracture and porous flow. Finally, simulations of 2-D plane strain hydraulic fracturing in porous media is offered and validated by the analytical solution from classical KGD model and Carter's equation. The example simulations demonstrate the applicability of proposed approach for modeling porous flow, fluid exchange at FSI, and hydraulic fracturing with leak-off effect.

The present work also bears certain limitations, which should be noted when applying or developing the computational approach. When modeling stiff solids, the fracture may appear to be thin and explicit modeling of the fluid inside fracture can be computationally demanding. Furthermore, the simulations presented herein assumes a pseudo-static condition where both fluid flow and fracture propagation is slow. For highly dynamic fracturing processes (e.g., [47]), the energy conservation properties of the fluid flow and fracturing process, the performance of the FSI model, and the wave dispersion properties of the poroelastic model, should all be further examined. Although outside the current scope of work, the proposed computational approach can be further developed to incorporate different FSI conditions accounting for the roughness of the fracture surface [92,93] and thermal field modeling [94] to cater for various scenarios encountered in engineering operations. It is also worth mentioning that other numerical approaches, such as phase-field [95] and coupled methods [96] were also reported capable in modeling fracturing in poroelastic media. It would be interesting and meaningful to study and compare the performance between different numerical methods in future studies.

CRediT authorship contribution statement

Zirui Lu: Writing – review & editing, Writing – original draft, Visualization, Validation, Software, Methodology, Investigation, Formal analysis, Data curation. **Fan Zhu:** Writing – review & editing, Writing – original draft, Supervision, Software, Project administration, Methodology, Funding acquisition, Conceptualization. **Yosuke Higo:** Writing – review & editing, Supervision, Resources. **Jidong Zhao:** Writing – review & editing, Methodology.

Declaration of competing interest

The authors declare that they have no known competing financial interests or personal relationships that could have appeared to influence the work reported in this paper.

Acknowledgments

This work was supported by JSPS KAKENHI Grant Number 23K13403.

Data availability

Data will be made available on request.

References

[1] C.T. Montgomery, M.B. Smith, Hydraulic fracturing: History of an enduring technology, J. Pet. Technol. 62 (12) (2010) 26–40.
[2] R.J. Davies, S.A. Mathias, J. Moss, S. Hustoft, L. Newport, Hydraulic fractures: How far can they go? Mar. Pet. Geol. 37 (1) (2012) 1–6.
[3] R. Moska, K. Labus, P. Kasza, Hydraulic fracturing in enhanced geothermal systems—field, tectonic and rock mechanics conditions—a review, Energies 14 (18) (2021) 5725.
[4] D.K. Shanmugam, T. Nguyen, J. Wang, A study of delamination on graphite/epoxy composites in abrasive waterjet machining, Composites A 39 (6) (2008) 923–929.
[5] R.A. Kerr, Learning how to NOT make your own earthquakes, Sci. 335 (2012) 1436–1437.
[6] F.H. Cornet, Earthquakes induced by fluid injections, Sci. 348 (6240) (2015) 1204–1205.
[7] J.I. Adachi, E. Detournay, Plane strain propagation of a hydraulic fracture in a permeable rock, Eng. Fract. Mech. 75 (16) (2008) 4666–4694.
[8] S. Salimzadeh, A. Paluszny, R.W. Zimmerman, Three-dimensional poroelastic effects during hydraulic fracturing in permeable rocks, Int. J. Solids Struct. 108 (2017) 153–163.
[9] R. Tanaka, M. Naoi, Y. Chen, K. Yamamoto, K. Imakita, N. Tsutsumi, A. Shimoda, D. Hiramatsu, H. Kawakata, T. Ishida, Preparatory acoustic emission activity of hydraulic fracture in granite with various viscous fluids revealed by deep learning technique, Geophys. J. Int. 226 (1) (2021) 493–510.

[10] L. Vandamme, J.H. Curran, A three-dimensional hydraulic fracturing simulator, Internat. J. Numer. Methods Engrg. 28 (4) (1989) 909–927.
[11] X. Zhang, R.G. Jeffrey, M. Thiercelin, Deflection and propagation of fluid-driven fractures at frictional bedding interfaces: a numerical investigation, J. Struct. Geol. 29 (3) (2007) 396–410.
[12] S. Cheng, M. Zhang, X. Zhang, B. Wu, Z. Chen, Z. Lei, P. Tan, Numerical study of hydraulic fracturing near a wellbore using dual boundary element method, Int. J. Solids Struct. 239 (2022) 111479.
[13] R.R. Settgast, P. Fu, S.D.C. Walsh, J.A. White, C. Annavarapu, F.J. Ryerson, A fully coupled method for massively parallel simulation of hydraulically driven fractures in 3-dimensions, Int. J. Numer. Anal. Methods Geomech. 41 (5) (2017) 627–653.
[14] B. Lecampion, An extended finite element method for hydraulic fracture problems, Commun. Numer. Methods Eng. 25 (2) (2009) 121–133.
[15] E. Gordeliy, A. Peirce, Coupling schemes for modeling hydraulic fracture propagation using the XFEM, Comput. Methods Appl. Mech. Engrg. 253 (2013) 305–322.
[16] T. Mohammadnejad, A.R. Khoei, An extended finite element method for hydraulic fracture propagation in deformable porous media with the cohesive crack model, Finite Elem. Anal. Des. 73 (2013) 77–95.
[17] Z. Sun, Z. Li, D.N. Espinoza, M.T. Balhoff, Fluid-driven fractures in granular media: Insights from numerical investigations, Phys. Rev. E 101 (4) (2020) 042903.
[18] L. Huang, E. Dontsov, H. Fu, Y. Lei, D. Weng, F. Zhang, Hydraulic fracture height growth in layered rocks: Perspective from DEM simulation of different propagation regimes, Int. J. Solids Struct. 238 (2022) 111395.
[19] X. Zhang, T. Hu, T. Man, Z. Ge, H.E. Huppert, Infiltration characteristics of slurries in porous media based on the coupled Lattice-Boltzmann discrete element method, Comput. Geotech. 177 (part A) (2025) 106865.
[20] T. Douillet-Grellier, R. Pramanik, K. Pan, A. Albaiz, B.D. Jones, H. Pourpak, J.R. Williams, Mesh-free numerical simulation of pressure-driven fractures in brittle rocks, in: SPE Hydraulic Fracturing Technology Conference and Exhibition, SPE, 2016, D011S001R004.
[21] S. Gharehdash, M. Barzegar, I.B. Palymskiy, P.A. Fomin, Blast induced fracture modelling using smoothed particle hydrodynamics, Int. J. Impact Eng. 135 (2020) 103235.
[22] Y.E. Aimene, J.A. Nairn, Modeling multiple hydraulic fractures interacting with natural fractures using the material point method, in: SPE/EAGE European Unconventional Resources Conference and Exhibition, SPE, 2014, D021S016R003.
[23] F. Sun, D. Liu, G. Wang, C. Cao, S. He, X. Jiang, S. Gong, Material point method simulation approach to hydraulic fracturing in porous medium, Eng. Anal. Bound. Elem. 162 (2024) 420–438.
[24] H. Ouchi, A. Katiyar, J. York, J.T. Foster, M.M. Sharma, A fully coupled porous flow and geomechanics model for fluid driven cracks: a peridynamics approach, Comput. Mech. 55 (2015) 561–576.
[25] S. Nadimi, I. Miscovic, J. McLennan, A 3D peridynamic simulation of hydraulic fracture process in a heterogeneous medium, J. Pet. Sci. Eng. 145 (2016) 444–452.
[26] S. Oterkus, E. Madenci, E. Oterkus, Fully coupled poroelastic peridynamic formulation for fluid-filled fractures, Eng. Geol. 225 (2017) 19–28.
[27] T. Ni, F. Pesavento, M. Zaccariotto, U. Galvanetto, Q.-Z. Zhu, B.A. Schrefler, Hybrid FEM and peridynamic simulation of hydraulic fracture propagation in saturated porous media, Comput. Methods Appl. Mech. Engrg. 366 (2020) 113101.
[28] X.P. Zhou, Y.T. Wang, Y.D. Shou, Hydromechanical bond-based peridynamic model for pressurized and fluid-driven fracturing processes in fissured porous rocks, Int. J. Rock Mech. Min. Sci. 132 (2020) 104383.
[29] W. Sun, J. Fish, F. Liu, Y. Lu, A stabilized two-phase PD-FEM coupling approach for modeling partially saturated porous media, Acta Geotech. 18 (2) (2023) 589–607.
[30] S.A. Silling, Reformulation of elasticity theory for discontinuities and long-range forces, J. Mech. Phys. Solids 48 (1) (2000) 175–209.
[31] S.A. Silling, M. Epton, O. Weckner, J. Xu, E. Askari, Peridynamic states and constitutive modeling, J. Elasticity 88 (2007) 151–184.
[32] T. Rabczuk, H. Ren, A peridynamics formulation for quasi-static fracture and contact in rock, Eng. Geol. 225 (2017) 42–48.
[33] F. Zhu, J. Zhao, Peridynamic modelling of blasting induced rock fractures, J. Mech. Phys. Solids 153 (2021) 104469.
[34] F. Bobaru, Y.D. Ha, W. Hu, Damage progression from impact in layered glass modeled with peridynamics, Cent. Eur. J. Eng. 2 (2012) 551–561.
[35] C.T. Wu, B. Ren, A stabilized non-ordinary state-based peridynamics for the nonlocal ductile material failure analysis in metal machining process, Comput. Methods Appl. Mech. Engrg. 291 (2015) 197–215.
[36] S.A. Silling, F. Bobaru, Peridynamic modeling of membranes and fibers, Int. J. Non-Linear Mech. 40 (2–3) (2005) 395–409.
[37] G. Zhang, Q. Le, A. Loghin, A. Subramaniyan, F. Bobaru, Validation of a peridynamic model for fatigue cracking, Eng. Fract. Mech. 162 (2016) 76–94.
[38] Z. Chen, F. Bobaru, Peridynamic modeling of pitting corrosion damage, J. Mech. Phys. Solids 78 (2015) 352–381.
[39] D. De Meo, C. Diyaroglu, N. Zhu, E. Oterkus, M.A. Siddiq, Modelling of stress-corrosion cracking by using peridynamics, Int. J. Hydrog. Energy 41 (15) (2016) 6593–6609.
[40] Y. Zhang, D. Huang, Z. Cai, Y. Xu, An extended ordinary state-based peridynamic approach for modelling hydraulic fracturing, Eng. Fract. Mech. 234 (2020) 107086.
[41] M. Qin, D. Yang, W. Chen, S. Yang, Hydraulic fracturing model of a layered rock mass based on peridynamics, Eng. Fract. Mech. 258 (2021) 108088.
[42] Y.W. Tsang, P.A. Witherspoon, Hydromechanical behavior of a deformable rock fracture subject to normal stress, J. Geophys. Res.: Solid Earth 86 (B10) (1981) 9287–9298.
[43] H. Fan, G.L. Bergel, S. Li, A hybrid peridynamics–SPH simulation of soil fragmentation by blast loads of buried explosive, Int. J. Impact Eng. 87 (2016) 14–27.
[44] H. Fan, S. Li, A Peridynamics-SPH modeling and simulation of blast fragmentation of soil under buried explosive loads, Comput. Methods Appl. Mech. Engrg. 318 (2017) 349–381.
[45] F. Yang, X. Gu, X. Xia, Q. Zhang, A peridynamics-immersed boundary-lattice Boltzmann method for fluid–structure interaction analysis, Ocean Eng. 264 (2022) 112528.
[46] X. Yao, D. Huang, Coupled PD-SPH modeling for fluid–structure interaction problems with large deformation and fracturing, Comput. Struct. 270 (2022) 106847.
[47] T. Ni, M. Mortazavi, A. Khoei, B.A. Schrefler, Mode I sub-and super-shear rupture and forerunning in porous media, Comput. Geotech. 171 (2024) 106372.
[48] M. Behzadinasab, J.T. Foster, A semi-Lagrangian constitutive correspondence framework for peridynamics, J. Mech. Phys. Solids 137 (2020) 103862.
[49] Q. Tu, S. Li, An updated Lagrangian particle hydrodynamics (ULPH) for Newtonian fluids, J. Comput. Phys. 348 (2017) 493–513.
[50] S.A. Silling, M.L. Parks, J.R. Kamm, O. Weckner, M. Rassaian, Modeling shockwaves and impact phenomena with Eulerian peridynamics, Int. J. Impact Eng. 107 (2017) 47–57.
[51] E. Madenci, A. Barut, M. Futch, Peridynamic differential operator and its applications, Comput. Methods Appl. Mech. Engrg. 304 (2016) 408–451.
[52] Y. Gao, S. Oterkus, Nonlocal numerical simulation of low Reynolds number laminar fluid motion by using peridynamic differential operator, Ocean Eng. 179 (2019) 135–158.
[53] Y. Gao, S. Oterkus, Fluid-elastic structure interaction simulation by using ordinary state-based peridynamics and peridynamic differential operator, Eng. Anal. Bound. Elem. 121 (2020) 126–142.
[54] X. Kan, J. Yan, S. Li, A. Zhang, On differences and comparisons of peridynamic differential operators and nonlocal differential operators, Comput. Mech. 68 (2021) 1349–1367.

[55] M. Gunzburger, R.B. Lehoucq, A nonlocal vector calculus with application to nonlocal boundary value problems, Multiscale Model. Simul. 8 (5) (2010) 1581–1598.
[56] Q. Du, M. Gunzburger, R.B. Lehoucq, K. Zhou, Analysis and approximation of nonlocal diffusion problems with volume constraints, SIAM Rev. 54 (4) (2012) 667–696.
[57] Q. Du, M. Gunzburger, R.B. Lehoucq, K. Zhou, A nonlocal vector calculus, nonlocal volume-constrained problems, and nonlocal balance laws, Math. Models Methods Appl. Sci. 23 (3) (2013) 493–540.
[58] Q. Du, M. Gunzburger, R.B. Lehoucq, K. Zhou, Analysis of the volume-constrained peridynamic Navier equation of linear elasticity, J. Elasticity 113 (2013) 193–217.
[59] G.L. Bergel, S. Li, The total and updated Lagrangian formulations of state-based peridynamics, Comput. Mech. 58 (2016) 351–370.
[60] C. Yang, F. Zhu, J. Zhao, Coupled total-and semi-Lagrangian peridynamics for modelling fluid-driven fracturing in solids, Comput. Methods Appl. Mech. Engrg. 419 (2024) 116580.
[61] A. Katiyar, J.T. Foster, H. Ouchi, M.M. Sharma, A peridynamic formulation of pressure driven convective fluid transport in porous media, J. Comput. Phys. 261 (2014) 209–229.
[62] R. Jabakhanji, R.H. Mohtar, A peridynamic model of flow in porous media, Adv. Water Resour. 78 (2015) 22–35.
[63] D.Z. Turner, A non-local model for fluid–structure interaction with applications in hydraulic fracturing, Int. J. Comput. Methods Eng. Sci. Mech. 14 (5) (2013) 391–400.
[64] Z. Chen, S. Niazi, F. Bobaru, A peridynamic model for brittle damage and fracture in porous materials, Int. J. Rock Mech. Min. Sci. 122 (2019) 104059.
[65] X. Song, S.A. Silling, On the peridynamic effective force state and multiphase constitutive correspondence principle, J. Mech. Phys. Solids 145 (2020) 104161.
[66] S. Menon, X. Song, A computational periporomechanics model for localized failure in unsaturated porous media, Comput. Methods Appl. Mech. Engrg. 384 (2021) 113932.
[67] X. Gu, X. Li, X. Xia, E. Madenci, Q. Zhang, A robust peridynamic computational framework for predicting mechanical properties of porous quasi-brittle materials, Compos. Struct. 303 (2023) 116245.
[68] X. Gu, L. Song, X. Xia, Yu. C., Finite element method-peridynamics coupled analysis of slope stability affected by rainfall erosion, Water 16 (15) (2024) 2210.
[69] M.A. Biot, General theory of three-dimensional consolidation, J. Appl. Phys. 12 (2) (1941) 155–164.
[70] J.R. Macdonald, Some simple isothermal equations of state, Rev. Modern Phys. 38 (4) (1966) 669.
[71] D. Tran, L. Nghiem, A. Settari, New iterative coupling between a reservoir simulator and a geomechanics module, SPE J. 9 (03) (2004) 362–369.
[72] S.A. Silling, E. Askari, A meshfree method based on the peridynamic model of solid mechanics, Comput. Struct. 83 (17–18) (2005) 1526–1535.
[73] H. Zhang, P. Qiao, A state-based peridynamic model for quantitative fracture analysis, Int. J. Fract. 211 (1) (2018) 217–235.
[74] H. Zhang, P. Qiao, A two-dimensional ordinary state-based peridynamic model for elastic and fracture analysis, Eng. Fract. Mech. 232 (2020) 107040.
[75] J. Yan, S. Li, X. Kan, A.M. Zhang, X. Lai, Higher-order nonlocal theory of Updated Lagrangian Particle Hydrodynamics (ULPH) and simulations of multiphase flows, Comput. Methods Appl. Mech. Engrg. 368 (2020) 113176.
[76] S. Li, W.K. Liu, Meshfree Particle Methods, Springer Science & Business Media, 2007.
[77] B.M. Das, S. Nagaratnam, Fundamentals of Geotechnical Engineering, Cengage Learning, 2017.
[78] M.A. Biot, Theory of elasticity and consolidation for a porous anisotropic solid, J. Appl. Phys. 26 (2) (1955) 182–185.
[79] R.E. Showalter, Diffusion in poro-elastic media, J. Math. Anal. Appl. 251 (1) (2000) 310–340.
[80] J. Mandel, Consolidation des sols (étude mathématique), Geotech. 3 (7) (1953) 287–299.
[81] S.Y. Yi, Convergence analysis of a new mixed finite element method for Biot's consolidation model, Numer. Methods Partial. Differ. Equ. 30 (4) (2014) 1189–1210.
[82] A.H.D. Cheng, E. Detournay, A direct boundary element method for plane strain poroelasticity, Int. J. Numer. Anal. Methods Geomech. 12 (5) (1988) 551–572.
[83] Y. Abousleiman, A.H.D. Cheng, C. Jiang, J.C. Roegiers, Poroviscoelastic analysis of borehole and cylinder problems, Acta Mech. 119 (1996) 199–219.
[84] P.J. Phillips, M.F. Wheeler, A coupling of mixed and continuous Galerkin finite element methods for poroelasticity I: the continuous in time case, Comput. Geosci. 11 (2007) 131–144.
[85] M. Ferronato, N. Castelletto, G. Gambolati, A fully coupled 3-D mixed finite element model of Biot consolidation, J. Comput. Phys. 229 (12) (2010) 4813–4830.
[86] R. Asadi, B. Ataie-Ashtiani, Numerical modeling of subsidence in saturated porous media: A mass conservative method, J. Hydrol. 542 (2016) 423–436.
[87] E. Holzbecher, Multiphysics modelling of the Mandel-Cryer effect, Int. J. Multiphys. 10 (1) (2016) 11–20.
[88] J. Geertsma, F. De Klerk, A rapid method of predicting width and extent of hydraulically induced fractures, J. Pet. Technol. 21 (12) (1969) 1571–1581.
[89] G.C. Howard, C.R. Fast, Optimum fluid characteristics for fracture extension, in: Drilling and Production Practice, OnePetro, 1957.
[90] J. Wang, D. Elsworth, M.K. Denison, Hydraulic fracturing with leakoff in a pressure-sensitive dual porosity medium, Int. J. Rock Mech. Min. Sci. 107 (2018) 55–68.
[91] A.P. Bunger, E. Detournay, D.I. Garagash, Toughness-dominated hydraulic fracture with leak-off, Int. J. Fract. 134 (2005) 175–190.
[92] D.B. Van Dam, C.J. De Pater, Roughness of hydraulic fractures: importance of in-situ stress and tip processes, Spe J. 6 (01) (2001) 4–13.
[93] B. Li, R. Liu, Y. Jiang, Influences of hydraulic gradient, surface roughness, intersecting angle, and scale effect on nonlinear flow behavior at single fracture intersections, J. Hydrol. 538 (2016) 440–453.
[94] C. Yang, F. Zhu, J. Zhao, A multi-horizon fully coupled thermo-mechanical peridynamics, J. Mech. Phys. Solids 191 (2024) 105758.
[95] S. Zhou, X. Zhuang, T. Rabczuk, A phase-field modeling approach of fracture propagation in poroelastic media, Eng. Geol. 240 (2018) 189–203.
[96] W. Sun, J. Fish, P. Lin, Numerical simulation of fluid-driven fracturing in orthotropic poroelastic media based on a peridynamics-finite element coupling approach, Int. J. Rock Mech. Min. Sci. 158 (2022) 105199.